J. Fluid Mech. (1976), *vol.* 75, *part* 1, *pp.* 113–148
Printed in Great Britain

Numerical simulation of three-dimensional Bénard convection in air

By FRANK B. LIPPS

Geophysical Fluid Dynamics Laboratory/NOAA, Princeton University, Princeton, New Jersey 08540

(Received 14 August 1974)

A numerical model is developed to simulate three-dimensional Bénard convection. This model is used to investigate thermal convection in air for Rayleigh numbers between 4000 and 25 000. According to experiments, this range of Rayleigh numbers in air covers three regimes of thermal convection: (i) steady two-dimensional convection, (ii) time-periodic convection and (iii) aperiodic convection. Numerical solutions are obtained for each of these regimes and the results are compared with the available experimental data and theoretical predictions.

At the Rayleigh number $Ra = 4000$ the present model is able to produce experimentally realistic wavelengths for the two-dimensional convection. The small amplitude wave disturbances at $Ra = 6500$ have period $\tau = 0{\cdot}24$. When they become finite amplitude travelling waves, the period is $\tau = 0{\cdot}27$. These values are in good agreement with theoretical and experimental results. A detailed study of the form of these waves and of their energetics is given in appendix A. As the Rayleigh number is increased to $Ra = 9000$ and 25 000, the convection manifests progressively more complex spatial and temporal variations.

The vertical heat transport and other mean properties of the convection are calculated for the range of Ra considered and compared with experimental and theoretical data. A detailed comparison is also made between the mean properties of two- and three-dimensional convection at the larger values of Ra. It is found that the heat flux Nu is nearly independent of the dimensionality of the convection.

1. Introduction

Many investigators have examined the dynamics of Bénard convection as the gravitational instability is increased. Perhaps the most definitive experimental description of this problem has been given by Krishnamurti (1970*a*, *b*, 1973), who discussed the increasing complexity of the flow patterns as the Rayleigh number is increased for a wide variety of fluids. Her data are summarized in figure 4 of Krishnamurti (1973), where the different flow regimes are mapped out in Prandtl number, Rayleigh number parameter space.

The present study is limited to Bénard convection in air for small and moderate values of the Rayleigh number Ra. For this case, the experimental work of Willis & Deardorff (1967, 1970) has to be considered of fundamental importance

as well. These experimentalists and Krishnamurti both found that the convection takes the form of quasi-steady two-dimensional flow for small values of Ra. When the Rayleigh number is increased to $Ra \simeq 5600$, three-dimensional time-periodic disturbances first appear. As the Rayleigh number was increased above $Ra \sim 12\,000$, Willis & Deardorff (1970) observed more complex spatial and temporal variations in the convection. For the present discussion this type of fluid motion will be called 'aperiodic' convection. When $Ra > 30\,000$, Willis & Deardorff found that the convection was sufficiently turbulent in appearance that well-defined thermal oscillations were rarely discernible at a given point.

A linear stability analysis of the onset of time-periodic disturbances was carried out by Busse (1972). His theory assumed conducting stress-free boundaries and was valid in the limit of vanishing Prandtl number, $Pr \to 0$. He found that the oscillatory instability is associated with the momentum advection terms in the equations of motion. These terms give rise to a vertical component of disturbance vorticity.

The above analysis was extended by Clever & Busse (1974) to include finite values of Pr. Conducting rigid boundaries were assumed so that the theoretical predictions could be compared with experimental data. The stability of two-dimensional rolls was tested with respect to the cross-roll, zig-zag and Eckhaus instabilities as well as the oscillatory instability. Using the observed wavelengths, Clever & Busse found that two-dimensional rolls are stable in air for $1708 \leqslant Ra < 6000$. When $Ra \geqslant 6000$, the oscillatory instability is present. The structure and periods of these theoretical disturbances are in excellent agreement with the experimental data. Clever & Busse also calculated the vertical heat transport associated with the roll solution for $2000 \leqslant Ra \leqslant 50\,000$.

In the present study a numerical model is developed which is capable of simulating three-dimensional thermal convection. This model is used to investigate the dynamics of Bénard convection in air for values of Ra between 4000 and 25 000. As indicated by the above discussion, the present range of Rayleigh numbers includes three regimes of thermal convection in air: (i) steady two-dimensional flow, (ii) three-dimensional time-periodic flow and (iii) aperiodic flow. Thus the present calculations are able to simulate a wide variety of convective motions over a relatively narrow interval of Rayleigh numbers.

The theoretical model for the present study is given in §2. This discussion includes the equations of motion, the energy equations and the numerical model. The results of the numerical calculations are presented in order of increasing Rayleigh number. The steady two-dimensional regime is discussed in §3. A detailed analysis of the calculated time-periodic disturbances at $Ra = 6500$ is given in §4 and appendix A. This analysis includes a description of the velocity and temperature fields, a discussion of the energetics, and a comparison of the present results with previous theoretical and experimental investigations. In §5 numerical simulations for $Ra = 9000$ and $Ra = 25\,000$ are presented. These solutions show increasingly complex space and time variations in the flow fields as the Rayleigh number is increased.

The mean statistics for Bénard convection in air are calculated in §6 for the interval $4000 \leqslant Ra \leqslant 25\,000$. The quantities obtained include volume-averaged

statistics such as the mean vertical heat flux and horizontally averaged statistics such as the variation of the mean temperature with height. The kinetic energy balance is calculated as a function of Ra. Also, the present results are compared with the existing experimental and theoretical data. A summary and the primary conclusions of this study are presented in § 7.

2. The theoretical model

In this investigation we examine the convection which develops in a fluid layer confined between two horizontal plates. The plates, separated by a distance d, are assumed to act as rigid, perfectly conducting boundaries. The unstable temperature difference $\Delta\theta$ between the boundaries is assumed to be much less than the mean temperature of the fluid layer. For this problem the kinematic viscosity ν, the thermal diffusivity κ and the coefficient of thermal expansion α may be treated as constants since the temperature variation is small. In addition, the Boussinesq approximation may be used (Chandrasekhar 1961, p. 16).

In the Bénard convection problem the fluid is usually assumed to be unbounded horizontally. However, the numerical model used in this study requires that some kind of boundary conditions be applied at lateral boundaries. The boundary conditions chosen should be such that they exert a minimum constraint on the fluid motions. In this investigation we assume that the flow is periodic at lateral boundaries.

2.1. *The equations of motion*

Cartesian co-ordinates are defined, with x' and y' horizontal and z' directed upwards. The corresponding velocity components are u', v' and w'. The primes indicate that the above variables are dimensional. The dimensionless variables are formed by using d, d^2/κ and $\Delta\theta$ as the scales for length, time and temperature respectively.

The four non-dimensional parameters relevant to the present problem are the Rayleigh number Ra, the Prandtl number Pr and the aspect ratios s_x and s_y:

$$Ra = g\alpha\Delta\theta d^3/\nu\kappa, \quad Pr = \nu/\kappa, \quad s_x = L_x/d, \quad s_y = L_y/d, \tag{1}$$

where g is the acceleration due to gravity and L_x and L_y are the horizontal dimensions of the present model. The existence of s_x and s_y indicates that the present problem has a finite horizontal domain. Also, since the present study is limited to Bénard convection in air at room temperature, $Pr = 0{\cdot}7$ for all cases.

Using the Boussinesq approximation, the dimensionless continuity, momentum and thermodynamic equations are

$$\nabla.\mathbf{V} = 0, \tag{2}$$

$$\frac{\partial\mathbf{V}}{\partial t}+\frac{\partial}{\partial x}(u\mathbf{V})+\frac{\partial}{\partial y}(v\mathbf{V})+\frac{\partial}{\partial z}(w\mathbf{V}) = -\nabla p + Pr\,Ra\,\theta\mathbf{k} + Pr\,\nabla^2\mathbf{V}, \tag{3}$$

$$\frac{\partial\theta}{\partial t}+\frac{\partial}{\partial x}(u\theta)+\frac{\partial}{\partial y}(v\theta)+\frac{\partial}{\partial z}(w\theta) = \nabla^2\theta, \tag{4}$$

where $\mathbf{V}$ is the velocity, θ is the temperature, p is the pressure and $\mathbf{k}$ is a unit vertical vector. The rigid conducting boundary conditions are $\mathbf{V} = 0$ and $\theta = \frac{1}{2}$ at $z = 0$ and $\mathbf{V} = 0$ and $\theta = -\frac{1}{2}$ at $z = 1$. The periodic side boundary conditions require cyclic continuity at $x = 0$ and $x = s_x$ and at $y = 0$ and $y = s_y$.

2.2. *The energy equations*

The total kinetic energy K and the total available potential energy P are defined by

$$K = \int_0^1 \tfrac{1}{2}\langle u^2 + v^2 + w^2\rangle \, dz, \tag{5a}$$

$$P = -Pr\, Ra \int_0^1 z\langle\theta\rangle \, dz, \tag{5b}$$

where angle brackets indicate an average over the entire horizontal domain. The equations for the time rates of change of K and P are

$$dK/dt = \{PK\} - D, \tag{6a}$$

$$dP/dt = -\{PK\} + PP, \tag{6b}$$

where $\{PK\}$, D and PP are defined as

$$\{PK\} = Pr\, Ra \int_0^1 \langle w\theta\rangle \, dz, \tag{6c}$$

$$D = Pr \int_0^1 \langle \nabla u . \nabla u + \nabla v . \nabla v + \nabla w . \nabla w\rangle \, dz, \tag{6d}$$

$$PP = Pr\, Ra \left[-\frac{d\langle\theta\rangle}{dz}\bigg|_{z=1} + \langle\theta\rangle|_{z=1} - \langle\theta\rangle|_{z=0} \right]. \tag{6e}$$

In these expressions, $\{PK\}$ is the conversion of potential energy into kinetic energy associated with the eddy transfer of heat $\langle w\theta\rangle$, D is the dissipation of kinetic energy by viscosity, and PP is the production of available potential energy due to diffusion of heat at the upper and lower boundaries.

A quantity closely related to the energetics is the total vertical heat flux. This quantity includes the heat flux due to both the eddies and the thermal diffusion. In a steady state, the total heat flux is independent of z. In that case the Nusselt number Nu is given by

$$Nu = -d\langle\theta\rangle/dz + \langle w\theta\rangle. \tag{7}$$

After integrating this equation once in the vertical we obtain

$$\{PK\} = Pr\, Ra\, (Nu - 1). \tag{8}$$

Thus Nu and $\{PK\}$ are linearly related in a steady state.

2.3. *The numerical model*

The numerical procedure for the time integration of (3) and (4) follows that described by Williams (1969). This procedure includes the solution of a numerical Poisson equation at each time step in order to obtain the pressure p. The present calculations have the simplification that Cartesian co-ordinates may be used whereas cylindrical co-ordinates are required in Williams's study. The present numerical model was used in the investigations of Lipps & Somerville (1971) and Somerville & Lipps (1973).

Run	Ra	s_x	s_y	T	N_x	N_y	N_z	N_t
A	4 000	6·00	4·91	12·89	44	36	16	5 460
B	4 000	6·00	4·67	8·21	36	28	14	3 420
C	6 500	4·00	3·20	10·26	28	20	14	8 550
D	9 000	4·00	3·50	5·43	36	32	18	6 030
E	25 000	3·90	3·90	2·38	40	40	20	4 770
F	6 500	2·00	3·20	9·65	20	32	20	12 060
$F1$	6 500	2·00	3·20	0·96	20	32	20	2 400

TABLE 1. Summary of primary numerical calculations for Bénard convection in air

The present calculations differ in a few respects from those described by Williams (1969). The nonlinear advective terms in (3) and (4) are put into the finite-difference form discussed by Piacsek & Williams (1970) for absolute quadratic conservation. The viscous and diffusive terms in (3) and (4) are calculated using the DuFort–Frankel difference scheme (Richtmyer & Morton 1967, p. 176). In Williams's procedure these terms were calculated at the lag time step.

The DuFort–Frankel scheme is stable for any value of the time step Δt, but is very inaccurate if Δt is large. This inaccuracy occurs because the DuFort–Frankel scheme introduces an artificial second time derivative into the finite-difference equations (Richtmyer & Morton 1967, p. 177). A detailed discussion of time and space truncation errors is given in appendix B. The advantage of using the DuFort–Frankel scheme is that at small Ra, where the time variation is relatively slow, a larger value of Δt may be used than would be possible if the viscous and diffusive terms were evaluated at the lag time step.

The primary numerical calculations in the present study are listed in table 1 and will be discussed in detail below. In this table T is the total non-dimensional time of the run, and N_x, N_y, N_z and N_t are the number of grid points in x, y, z and t respectively. The corresponding grid intervals Δx, Δy, Δz and Δt for the numerical runs A–$F1$ are given in table 5 in appendix B.

3. The two-dimensional regime

Bénard convection in air is first examined for values of Ra in the interval $1708 < Ra < 5600$, where the flow is observed to be quasi-two-dimensional and steady. For this problem it might be thought that a two-dimensional numerical model would be sufficient to study the dynamics of the convection. If, however, the correct wavelength for the rolls is to be obtained from solving an initial-value problem, a three-dimensional numerical model is required (Lipps & Somerville 1971). This is because the transient motion leading up to the asymptotic two-dimensional steady state is three-dimensional. If a two-dimensional model is used to obtain solutions for the initial-value problem, the calculated wavelengths of the rolls will be smaller than is experimentally observed.

An example of such an initial-value calculation is run A in table 1. This calculation was carried out for $Ra = 4000$ with the aspect ratios $s_x = 6{\cdot}00$ and $s_y = 4{\cdot}91$.

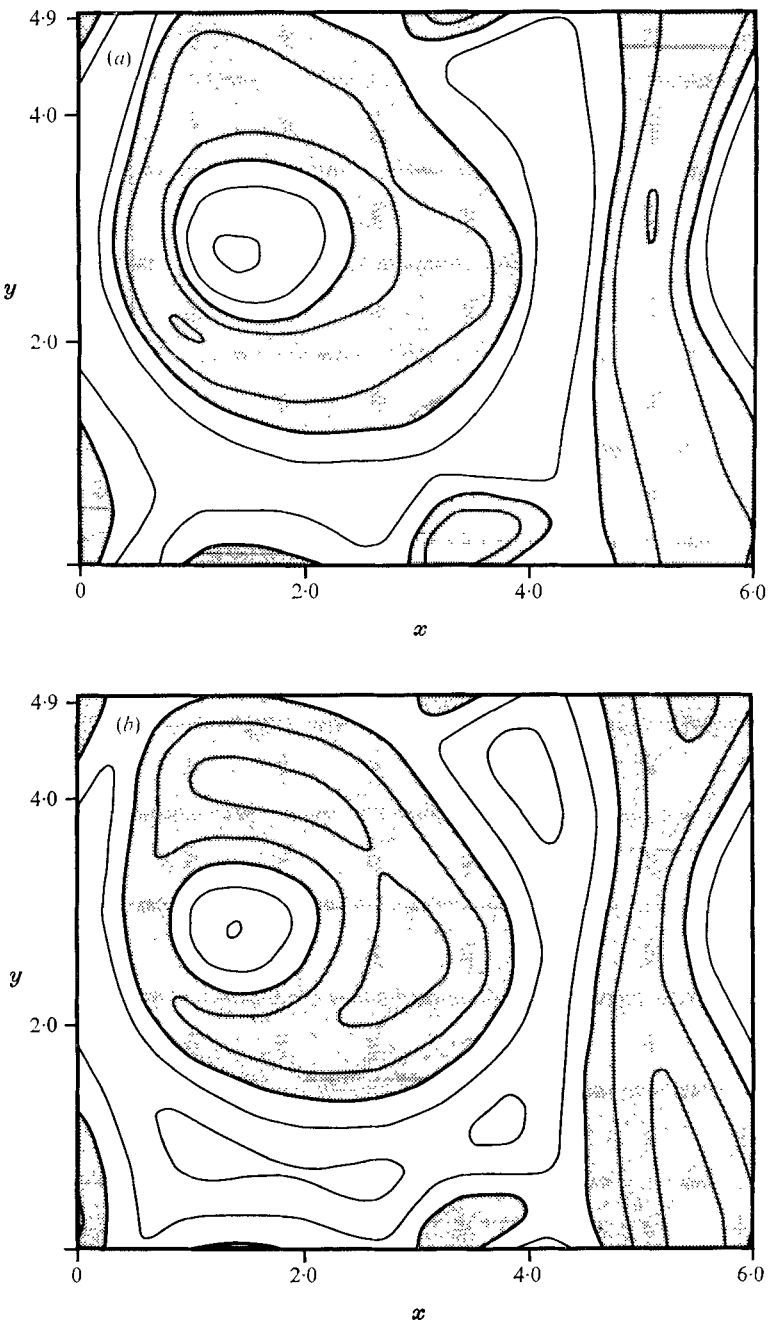

FIGURE 1. (*a*) Isotachs of vertical velocity w and (*b*) isotherms of temperature θ in the x, y plane for $Ra = 4000$. This cross-section is for the mid-level $z = \frac{1}{2}$ at $t = 4{\cdot}39$ in run A. Heavy lines separate areas of positive and negative w or θ. The stippled areas are negative. The contour interval is 7·5 for w and 0·15 for θ.

The initial conditions require the air to be at rest ($\mathbf{V} = 0$) and the temperature θ to be given by the conductive solution with a random disturbance superimposed upon it. Because of the thermal instability many cells formed at the beginning of the run. As the run progressed, many of these cells combined, so that the horizontal scale of the disturbances increased. In figures 1 (*a*) and (*b*) the fields of w and θ at $z = \frac{1}{2}$ are shown at the non-dimensional time $t = 4{\cdot}39$. On the left side of the horizontal domain there is a strong cell of positive w and θ surrounded by concentric contours of negative w and θ. After $t = 4{\cdot}39$ this positive cell began to weaken slowly. At about $t \simeq 9{\cdot}2$ another positive cell formed near the upper left-hand corner of the domain. This cell then decayed slowly. As it did so, rolls formed on the left side of the domain, parallel to y. At the end of the run, $t = T = 12{\cdot}89$, the pattern was fully two-dimensional with rolls parallel to y. The wavenumber n_x of this final flow field was $n_x = 2$, which corresponds to a wavelength $\lambda_{\text{num}} = 3{\cdot}00$. This calculation (run A) was discussed briefly in Lipps & Somerville (1971). A similar calculation was performed by Somerville (1973), who also obtained $\lambda_{\text{num}} = 3{\cdot}00$.

A second calculation (run B) was carried out at $Ra = 4000$, with $s_x = 6{\cdot}00$, $s_y = 4{\cdot}67$ and a slightly poorer spatial resolution (table 5). After calculations had been performed for a non-dimensional time $t = 8{\cdot}21$, the flow field was again approaching a two-dimensional steady state. The geometry of this flow field was such that $n_x = 2$ and $n_y = 1$, so that the wavelength was given by $\lambda_{\text{num}} = 2{\cdot}52$.

Although two cases do not represent an adequate statistical sample, it may be seen that the average value of λ_{num} at $Ra = 4000$ from runs A and B is close to the experimental value $\lambda_{\text{exp}} = 2{\cdot}8$ given by Willis, Deardorff & Somerville (1972). It should be noted that the experimental wavelength was obtained as an average over many experimental realizations. The dynamics of this wavelength selection are not understood. Apparently, the dynamics are reproduced in a three-dimensional model as here, but not in a two-dimensional model.

The numerical calculations at $Ra = 4000$ did not exhibit the very slow time oscillations discussed by Willis & Deardorff (1967, 1970). The absence of these oscillations may be due to the time and horizontal domain limitations of the numerical model. The period of these slow oscillations has a non-dimensional value of about ten.

4. Onset of three-dimensional disturbances

It is observed that three-dimensional time-periodic disturbances develop when the Rayleigh number exceeds $Ra \simeq 5600$. These disturbances first appear as small amplitude waves superimposed on the finite amplitude two-dimensional rolls. They can take the form either of standing waves or of travelling waves which propagate along the rolls. The present numerical model has been used to investigate the dynamics and energetics of these disturbances.

When the Rayleigh number is increased above $Ra = 5600$, higher grid resolutions are needed, and it is therefore no longer feasible to prescribe a large enough horizontal domain so that the convection has sufficient freedom in 'choosing' the preferred scale. Thus a compromise was made for values of Ra above

$Ra = 5600$: a roll width close to that given by Willis *et al.* (1972) was prescribed in the initial conditions, but the fluid was allowed to 'choose' the wavelength of the three-dimensional disturbance superimposed upon the roll.

Specifically, when $Ra \geqslant 6500$, the initial conditions were that (i) the fluid is at rest ($\mathbf{V} = 0$) and (ii) the temperature θ is given by

$$\theta(x, y, z, 0) = 0{\cdot}5 - z + 0{\cdot}1 \sin(2\pi y/s_y) \sin(\pi z) + \theta_r, \tag{9}$$

where θ_r is a small random temperature disturbance. For sufficiently large values of s_x, the above initial conditions allow the fluid the freedom to 'choose' the wavelength λ_x of the disturbances which form along the rolls. In practice, however, the values of s_x were about twice the expected values of λ_x. Thus the present resolution allowed limited freedom in the selection of λ_x.

4.1. *Onset of travelling waves at* $Ra = 6500$

The first numerical experiment carried out with the above initial conditions was run C in table 1, at $Ra = 6500$. The horizontal domain is given by $s_x = 4{\cdot}00$ and $s_y = 3{\cdot}20$. After a non-dimensional time $t = 3{\cdot}0$, clearly defined small amplitude wave disturbances are superimposed upon the finite amplitude rolls. These disturbances have a wavenumber $n_x = 2$, or a wavelength in the x direction of $\lambda_x = 2{\cdot}0$. At this early stage in their development the disturbances seem to be primarily standing waves with a period $\tau = 0{\cdot}25$. Near the end of the run the disturbances are travelling waves with the period $\tau = 0{\cdot}28$. These have constant amplitude, so that a steady state exists in a co-ordinate system moving with the waves. Fields of w and θ at $z = 0{\cdot}5$ are shown in figure 2 for the end of run C ($T = 10{\cdot}26$). The wavy patterns in this figure move from right to left, indicating a negative phase velocity c_x.

Figure 3 shows the fields of w and θ in the y, z plane. These cross-sections are for the value of x indicated by the arrow in figure 2. The variables w and θ are shown at two different times, $t = 10{\cdot}17$ and $t = 10{\cdot}26$. Since the period of the oscillations is $\tau = 0{\cdot}28$, this time interval represents nearly one-third of a period. The w and θ fields plotted at $t = 10{\cdot}17$ show these variables just after their maximum displacement towards smaller values of y while the fields plotted at $t = 10{\cdot}26$ show these variables just prior to their maximum displacement towards larger values of y. It appears that, as the wave patterns move along the rolls, the vertical velocity field is more strongly affected by the disturbances than is the temperature field. This tendency is seen in both figure 2 and figure 3.

The present value of λ_x can be compared with results from the stability analysis of Clever & Busse (1974). For a roll wavelength of $\lambda_y = \pi$, the data in figure 8 of their study show that the most unstable wavelength is $\lambda_x = 2{\cdot}6$ at $Ra = 6500$. The value $\lambda_x = 2{\cdot}0$ found above is strongly influenced by the choice of $s_x = 4{\cdot}00$.

4.2. *Energetics at* $Ra = 6500$

The data for the energetics are taken from runs F and $F1$ in table 1. For both of these runs the horizontal domain is given by $s_x = 2{\cdot}00$ and $s_y = 3{\cdot}20$. The wavenumber of the disturbances in the x direction is $n_x = 1$, so that the wavelength remains $\lambda_x = 2{\cdot}0$. The energetics are calculated from these runs instead of run C

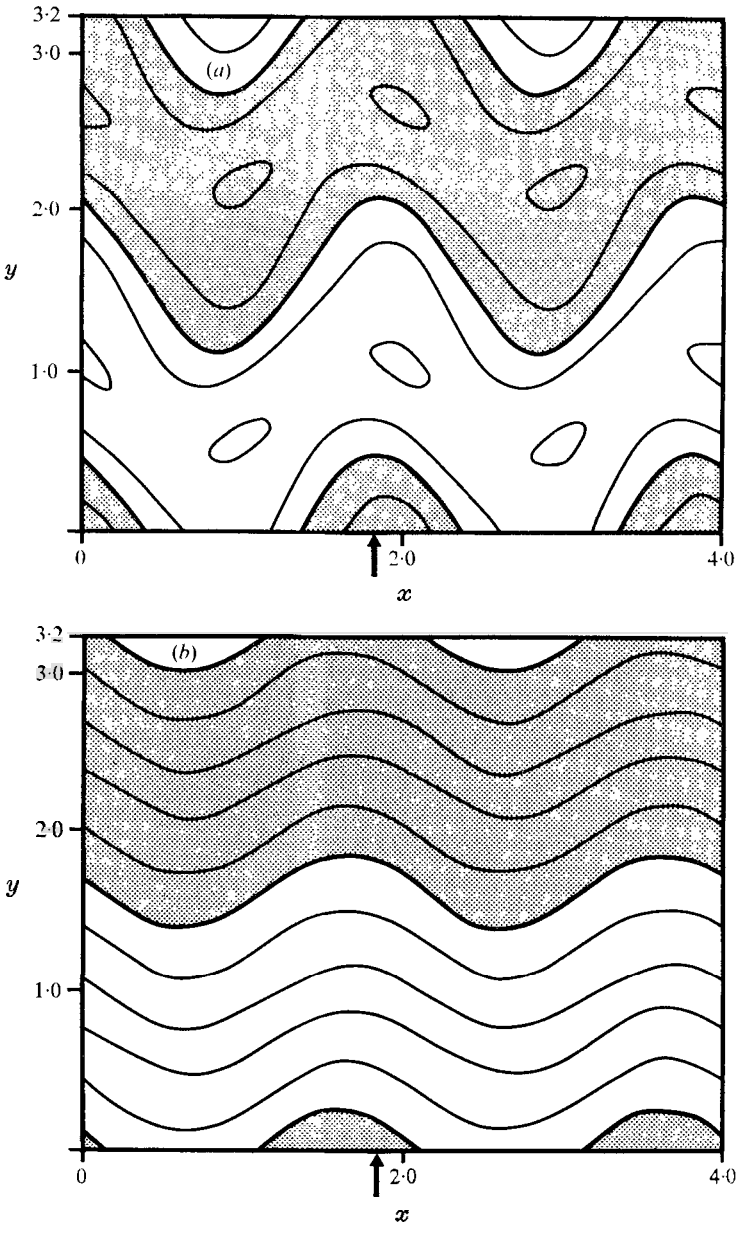

FIGURE 2. (*a*) Isotachs of vertical velocity w and (*b*) isotherms of temperature θ in the x, y plane for $Ra = 6500$. This cross-section is for $z = \frac{1}{2}$ at the end of run C ($t = 10{\cdot}26$). The contour interval is 7·5 for w and 0·15 for θ. The arrow indicates the value of x for the y, z cross-sections shown in figure 3. Stippled areas are negative.

because the numerical space and time truncation errors are less. Thus the quantitative data will be more accurate. A detailed discussion of the numerical truncation errors associated with the three runs C, F and $F1$ is given in appendix B.

The initial conditions for run F were the same as those used for run C. The two-dimensional roll solution came into equilibrium after a time $t \simeq 0{\cdot}60$. By the

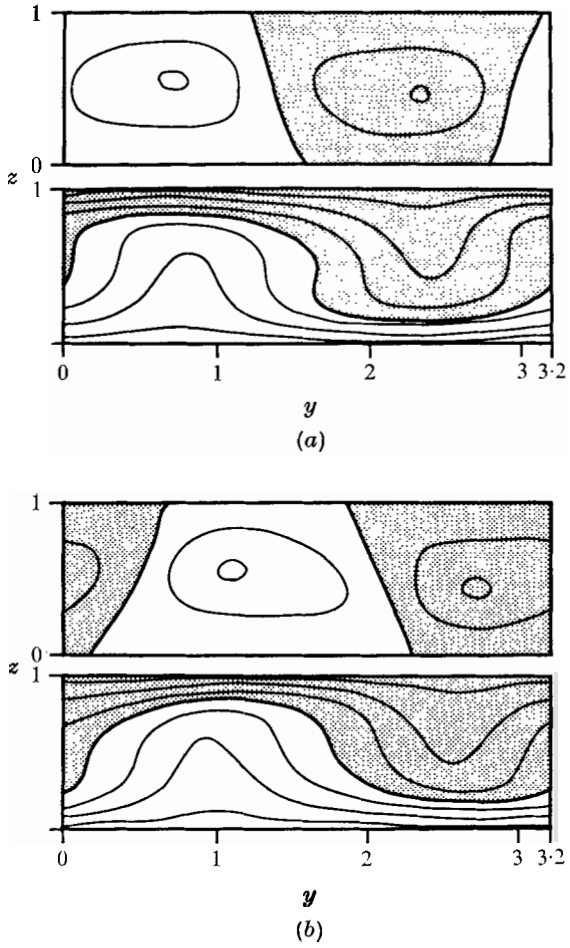

FIGURE 3. Cross-sections of w (upper diagram of each pair) and θ (lower diagram) in the y, z plane for $Ra = 6500$ from run C. (*a*) $t = 10{\cdot}17$. (*b*) $t = 10{\cdot}26$. The contour interval is 7·5 for w and 0·15 for θ. Stippled areas are negative.

time $t \simeq 2{\cdot}50$, the wave disturbances had become organized and were very small and growing. The energetics at this time were still dominated by the finite amplitude two-dimensional roll solution. The values of K, P, Nu, $\{PK\}$ and τ are shown in table 2 for $t \simeq 2{\cdot}50$ for run F. After run F had been completed ($T = 9{\cdot}65$), the final values of V and θ were used as the initial conditions in run $F1$. At the end of run $F1$ ($T = 0{\cdot}96$), the energetics of the convection with both the rolls and the finite amplitude travelling waves were in a steady state. The values of K, P, Nu, $\{PK\}$ and τ for these fully developed wave disturbances are also given in table 2.

The data shown in table 2 indicate that the development of travelling waves with $\lambda_x = 2{\cdot}0$ at $Ra = 6500$ slightly decreases the intensity of the convection. Consistent with this interpretation, the values of K, Nu and $\{PK\}$ are smaller and P is larger when finite amplitude travelling waves are present. These detailed results, however, may not be the same for other values of λ_x. In a more general sense, the data in table 2 suggest that the energetics are relatively insensitive to

	K	P	Nu	$\{PK\}$	τ
Onset value	86·9	251	2·08	4910	0·24
Final value	86·7	256	2·05	4780	0·27

TABLE 2. The values of K, P, Nu, $\{PK\}$ and τ at $Ra = 6500$ from runs F and $F1$. The upper row of values is taken at the time $t \simeq 2{\cdot}50$ from run F. The lower row is taken from the end of run $F1$.

the existence of time-periodic disturbances. This conclusion is consistent with the data for K and Nu in table 3 and the discussion in §6.2.

The values of τ in table 2 are virtually the same as those obtained previously for run C. The present values can be compared with previous experimental and theoretical results. From figure 9 of Willis & Deardorff (1970), the experimental value $\tau = 0{\cdot}32$ at $Ra = 6500$ is obtained. This value is best compared with the final value $\tau = 0{\cdot}27$, when the numerical disturbances were of finite amplitude. Theoretical values of τ can be found from figure 8 of Clever & Busse (1974). The value $\tau = 0{\cdot}23$ is obtained for $\lambda_y = \pi$, $\lambda_x = 2{\cdot}0$ and $Ra = 6500$. This value is best compared with the onset value, $\tau = 0{\cdot}24$, when the numerical disturbances were very small. Thus the numerical values of τ are in good agreement with experimental and theoretical results.

The energetics and dynamics of the disturbances are discussed in greater detail in appendix A, where the total flow field is separated into the mean flow (average taken along x) and the disturbance flow. Thus the total kinetic energy K is separated into a mean flow kinetic energy $\overline{K}$ associated with the rolls and a disturbance kinetic energy K' associated with the oscillations. The primary conclusions from appendix A are summarized in §7.

One result that can be discussed here is the relationship between τ and the mean flow kinetic energy $\overline{K}$. According to Busse & Whitehead (1974), the period τ is proportional to the circulation time of the mean flow. In the present problem the wavelength λ_y of the mean flow is held fixed. For this discussion, we assume that the spatial variation of the mean flow is virtually unchanged for modest changes in $\overline{K}$. Under these conditions, the statement by the above authors can be represented by the relation $\tau \propto \overline{K}^{-\frac{1}{2}}$. At the onset of the disturbances, $\tau = 0{\cdot}24$ and $K = \overline{K} = 86{\cdot}9$ as given in table 2. When the disturbances reach finite amplitude, $\tau = 0{\cdot}27$ and $\overline{K} = 62{\cdot}8$ (as given in figure 14). These two sets of values are compatible with the relationship $\tau \propto \overline{K}^{-\frac{1}{2}}$ to within 5 %.† Thus the present data also imply that τ is proportional to the circulation time of the mean flow.

5. Convection at higher Rayleigh numbers

The two remaining numerical solutions to be discussed are for the Rayleigh numbers $Ra = 9000$ and $Ra = 25\,000$. These calculations are denoted in table 1 as runs D and E. The initial conditions are as in run C, where $\mathbf{V} = 0$ and the temperature θ is given by (9).

† The same result is obtained if an extra decimal place is retained in the calculated values of τ.

At $Ra = 9000$ the convection is still essentially periodic in time. When the Rayleigh number was increased above $Ra = 12\,000$, Willis & Deardorff (1970) observed that more complicated time-dependent motions became increasingly frequent. These motions took the form of breaking waves and isolated sharp-crested waves of short wavelength. These types of aperiodic motion are seen in the numerical solution at $Ra = 25\,000$.

5.1. *Time-periodic convection at* $Ra = 9000$

The horizontal aspect ratios for run D are given by $s_x = 4{\cdot}00$ and $s_y = 3{\cdot}50$. With the above initial conditions, rolls parallel to the x axis quickly formed with the wavelength $\lambda_y = 3{\cdot}5$. By $t \simeq 0{\cdot}90$ travelling wave disturbances had formed with a negative phase velocity c_x and a wavelength $\lambda_x = 2{\cdot}0$. These waves had a period $\tau = 0{\cdot}26$ and their amplitude was nearly the same whether they were travelling upon the middle roll (centred at $y = \frac{1}{2}s_y$) or upon the outside roll (centred at $y = 0$ or $y = s_y$). At $t \simeq 1{\cdot}00$, however, the amplitude of the disturbances became larger on the centre roll. After some transient effects, the large amplitude disturbances then moved to the outside roll at $t \simeq 2{\cdot}5$ and remained there until the end of run D.

At $t \simeq 2{\cdot}2$ the disturbances started moving at different phase speeds on the two rolls. The larger amplitude disturbances on the outside roll moved more slowly than the weaker disturbances on the centre roll. The difference in phase velocities increased from $t \simeq 2{\cdot}2$ until $t \simeq 3{\cdot}8$. From $t \simeq 3{\cdot}8$ until the end of the run ($t = 5{\cdot}43$) the phase velocities of the disturbances changed relatively little. At the end of the run the period of the weaker disturbances on the centre roll was $\tau \simeq 0{\cdot}24$ while the much larger amplitude disturbances on the outside roll had period $\tau \simeq 0{\cdot}45$.

Figure 4 shows the fields of w and θ at the $z = \frac{1}{2}$ mid-level for the end of the run. Again, the disturbances in the w field appear to have larger relative amplitude than those in θ. In figure 5 vertical cross-sections of the w and θ fields in the x, z plane are shown for $y = 0$. These cross-sections cut through the centre of the outside roll, where the travelling waves have the larger amplitude and longer period. Figure 6 shows the corresponding cross-sections at $y = \frac{1}{2}s_y$ for the weaker disturbances superimposed upon the centre roll. Here it is seen that the flow is more complex than a simple $n_x = 2$ periodicity in x. The first cell for positive w and the last cell for negative w are clearly somewhat stronger than the two middle cells for w.

The time variation of w and θ at two specific points on the plane $z = \frac{1}{2}$ is shown in figure 7. The first of these is at $y = 0$, at point A in figure 4. Here the outside-roll disturbances have maximum amplitude. It is seen that the wave patterns on this roll are relatively periodic. The second point is located on the centre roll at $y = \frac{1}{2}s_y$, at point B in figure 4. Here the time variation of w and θ is more irregular. It should be noted that the periods $\tau \simeq 0{\cdot}24$ for the centre-roll disturbances and $\tau = 0{\cdot}45$ for the outside-roll disturbances were obtained as mean values from the two time variations of w shown in this figure.

Somerville (1973) also carried out a numerical simulation at $Ra = 9000$ and obtained travelling wave solutions. His calculations, however, were not reported to give the varying phase speed and amplitude of the travelling waves found above.

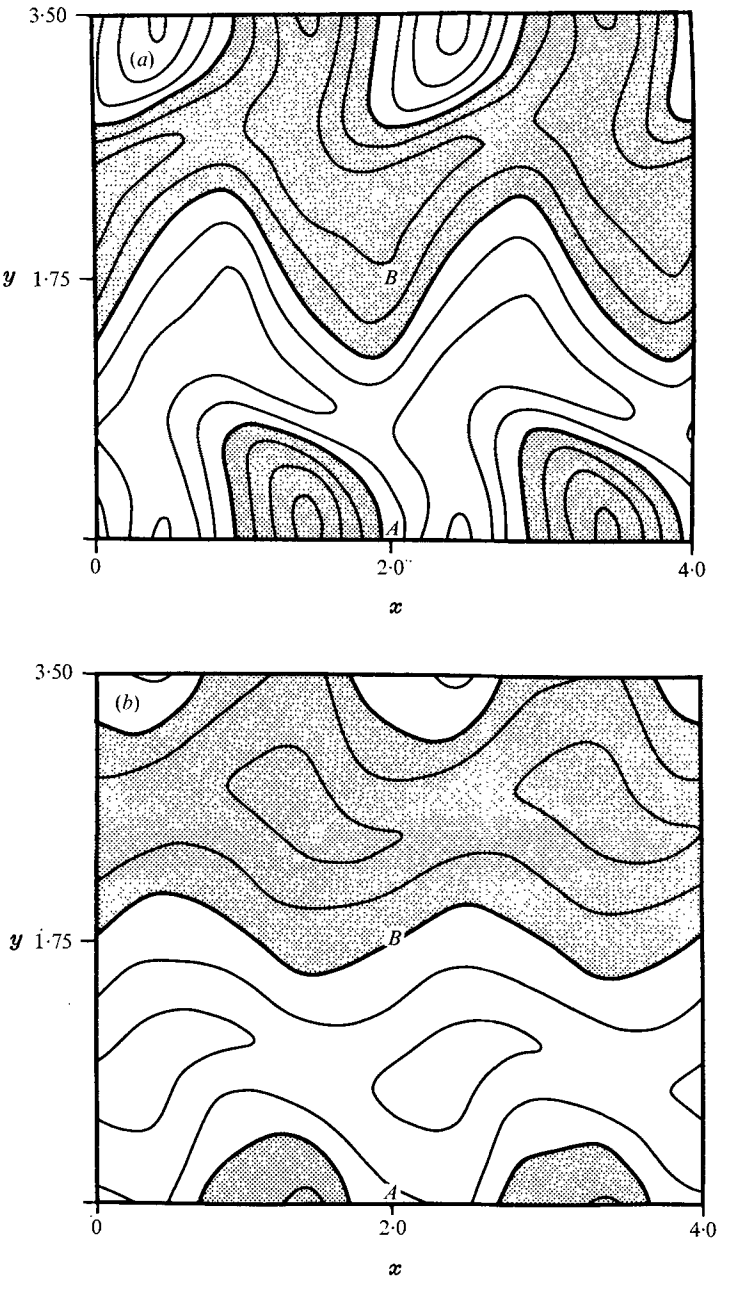

FIGURE 4. (*a*) Isotachs of vertical velocity w and (*b*) isotherms of temperature θ in the x, y plane for $Ra = 9000$. This cross-section is shown for $z = \frac{1}{2}$ at the end of run D. The contour interval is 7·5 for w and 0·15 for θ. Stippled areas are negative. The two points at which w and θ are shown as functions of time in figure 7 are indicated by A and B.

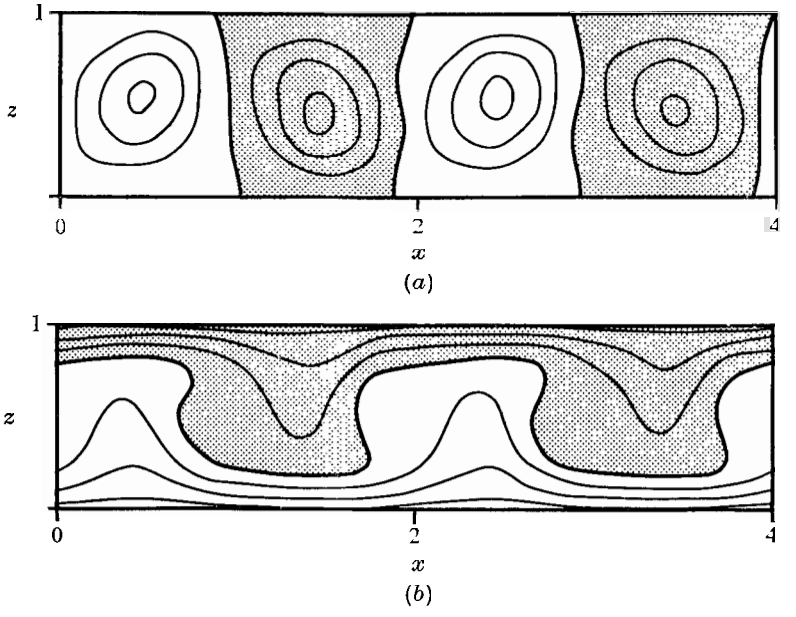

FIGURE 5. Cross-sections of (*a*) w and (*b*) θ in the plane $y = 0$ for $Ra = 9000$. Stippled areas are negative. The contour interval is 7·5 for w and 0·15 for θ.

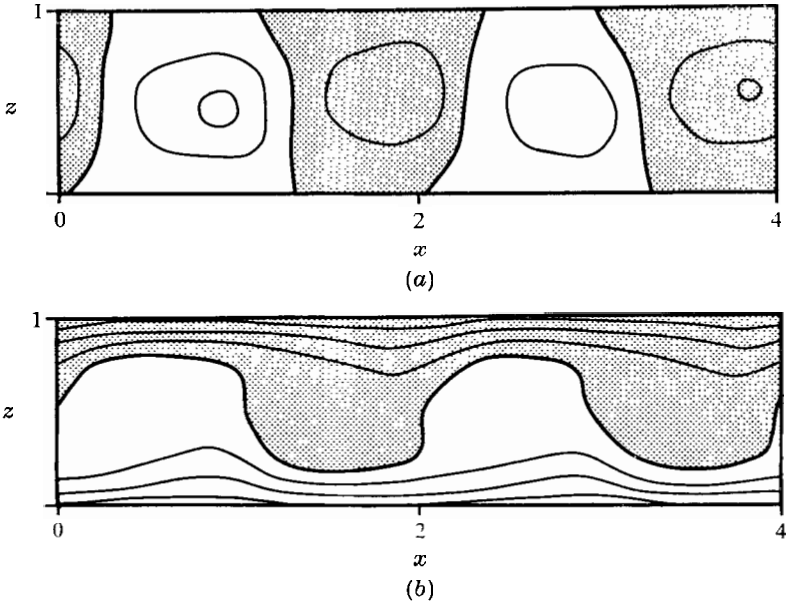

FIGURE 6. Cross-sections of (*a*) w and (*b*) θ in the plane $y = \frac{1}{2}s_y$ for $Ra = 9000$. Stippled areas are negative. The contour interval is 7·5 for w and 0·15 for θ.

5.2. *Aperiodic convection at* $Ra = 25\,000$

The horizontal aspect ratios for run E are $s_x = 3{\cdot}90$ and $s_y = 3{\cdot}90$. For the present initial conditions, rolls parallel to the x axis with the wavelength $\lambda_y = 3{\cdot}9$ were expected to develop. However, as seen below, a more complicated time-dependent

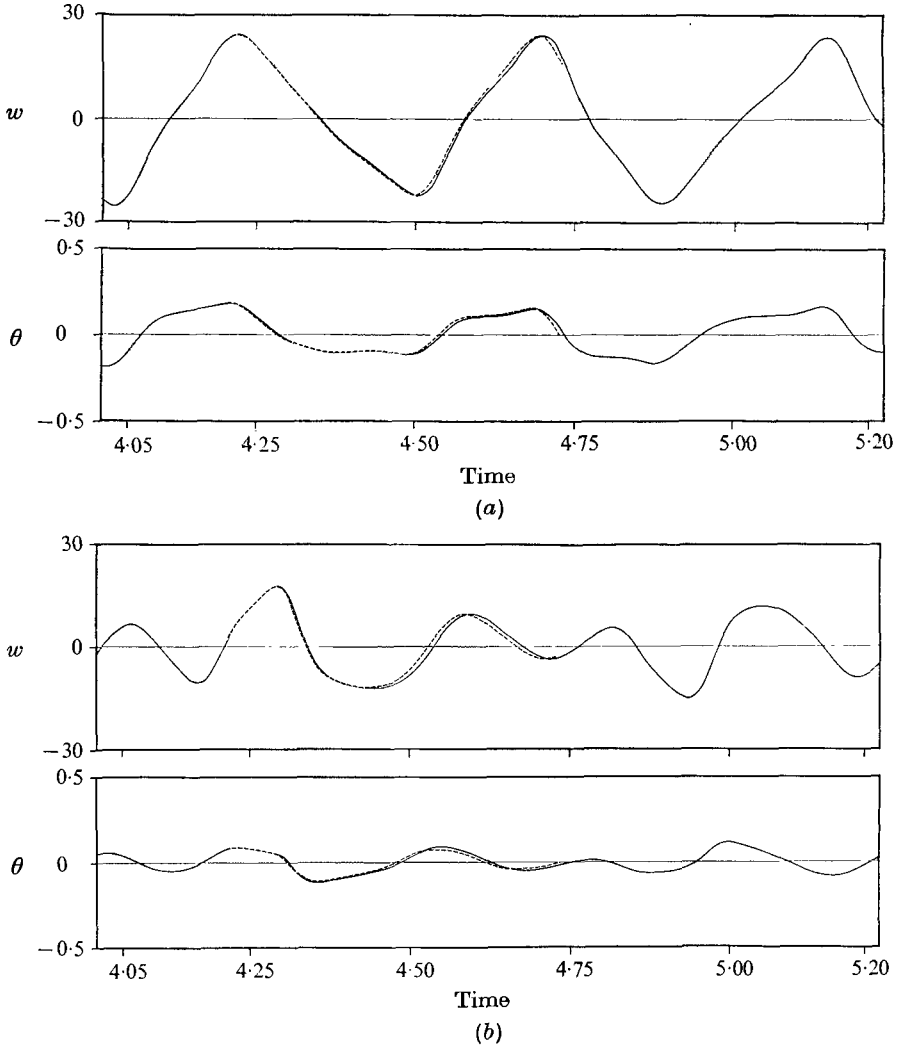

FIGURE 7. Time variation of w and θ on the mid-level $z = \frac{1}{2}$ for $Ra = 9000$ at the points denoted by (*a*) A and (*b*) B in figure 4. ——, results obtained from run D; – – –, time variation when the time step Δt was reduced by one-half (see appendix B).

three-dimensional pattern evolved. The wavelength $\lambda_y = 3{\cdot}9$ is in good agreement with the recent data given by Willis *et al.* (1972).

Early in this run the rolls with the wavelength $\lambda_y = 3{\cdot}9$ were better organized and thus started developing more rapidly than the disturbances. By $t \simeq 0{\cdot}18$, however, wavelike w disturbances were becoming of large amplitude at the level $z = \frac{1}{2}$. There was a tendency for tongues of positive and negative w to form parallel to the y axis, normal to the rolls. The wavenumber of this x-dependent motion was $n_x \approx 2$. The thermal oscillations were again considerably weaker in amplitude than the vertical velocity fluctuations.

By the time $t \simeq 0{\cdot}32$, w cells of large amplitude were lined up more nearly parallel to the y axis than the x axis. The θ field was now highly disturbed, but

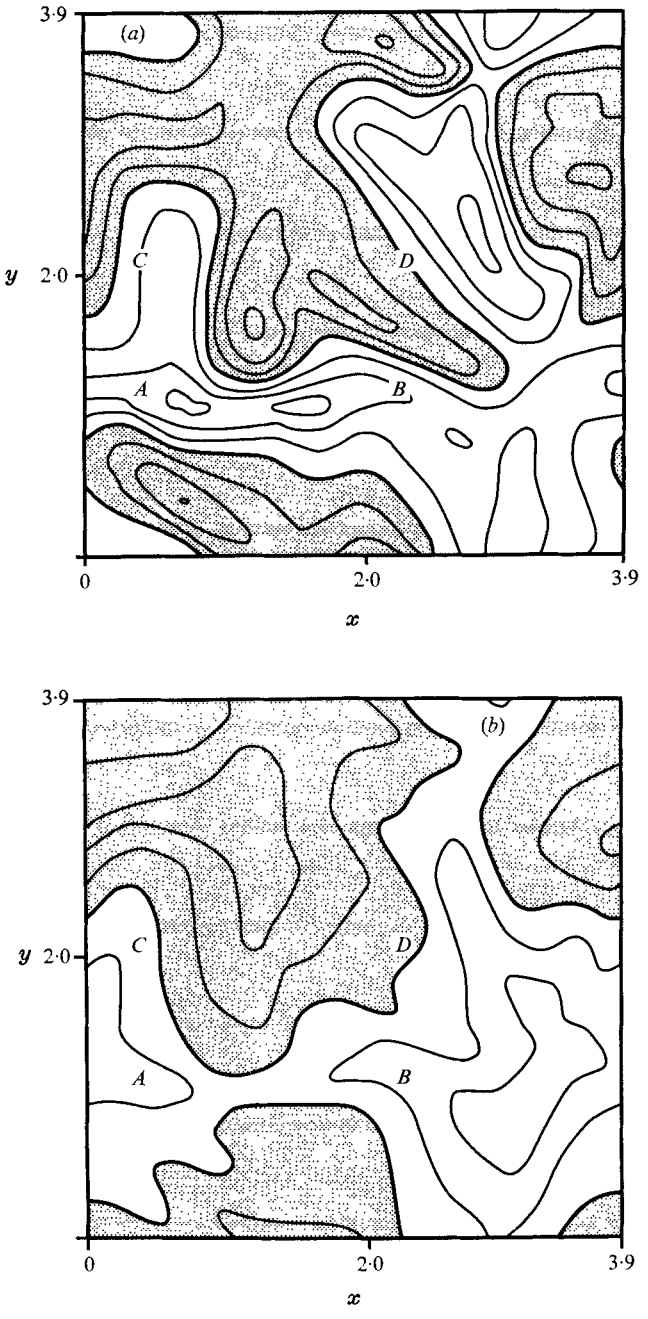

FIGURE 8. (*a*) Isotachs of vertical velocity w and (*b*) isotherms of temperature θ in the x, y plane for $Ra = 25\,000$. This figure is for $z = \frac{1}{2}$ at $t = 2{\cdot}205$. The contour interval is 15·0 for w and 0·15 for θ. Stippled areas are negative. The four points at which w and θ are shown as functions of time in figure 10 are indicated by A, B, C and D.

still lined up more nearly parallel to the x axis as in the original rolls. As the w oscillations continued to grow, the roll-like thermal disturbances at both $y \simeq \frac{1}{4}s_y$ and $y \simeq \frac{3}{4}s_y$ became broken by narrow regions of temperature θ of the opposite sign to that of the original rolls. These narrow regions correspond to intense vertical velocity cells lined up parallel to y. This type of convective motion appears to be very similar to the breaking wave motion discussed by Willis & Deardorff (1970). They observed that for $Ra > 12\,000$ fluid at the crest of one oscillating roll would occasionally spill into the next roll with vorticity of the same sign.

When $t \simeq 0{\cdot}46$, the θ field started looking more like the fully developed temperature field, with a cell of minimum temperature located near $x = 1{\cdot}2$, $y = 3{\cdot}2$ and a cell of maximum temperature located near $x = 3{\cdot}2$, $y = 1{\cdot}3$ at the level $z = \frac{1}{2}$ (see figure 8). The w field at this time was still very closely parallel to y. By $t \simeq 0{\cdot}60$ the w field was considerably less parallel to y and both fields started exhibiting the types of patterns characteristic of the remainder of the run.

A typical example of the w and θ fields at the level $z = \frac{1}{2}$ is shown in figures 8 (a) and (b) for the time $t = 2{\cdot}205$. For this case the upward vertical velocity appears to be dominant with a roll-like feature across the horizontal region at $y \approx 1{\cdot}1$. Another area of positive vertical velocity cuts across the horizontal region at $x \approx 2{\cdot}8$. These regions of upward velocity in figure 8 (a) correspond to regions of positive temperature in figure 8 (b). However, the most prominent features in figure 8 (b) are the positive temperature cell towards the lower right and the negative temperature cell in the upper left portion of this figure. These two cells are semi-permanent features of the present run at $Ra = 25\,000$.

The type of semi-cross-roll pattern with positive vertical velocity in the roll-like disturbances was observed during a large part of the present numerical experiment. This flow pattern was dominant early in the run, from $t \simeq 0{\cdot}6$ until $t \simeq 1{\cdot}3$, and later, from $t \simeq 1{\cdot}7$ until $t \simeq 2{\cdot}34$. In between these times a similar cross-roll pattern tended to be dominant but with negative vertical velocity in the roll-like disturbances. In that case the positive and negative temperature cells were still present, but both were displaced towards larger values of x and y relative to the temperature cells shown in figure 8 (b). The above time variations suggest a period of $\tau \simeq 1{\cdot}3$ for the cross-roll pattern.

The short-term variations in the convection are examined by comparing the w and θ fields at $z = \frac{1}{2}$ shown in figures 8 (a) and (b) with the same fields at a time $\delta t = 0{\cdot}03$ later. The later fields, at the time $t = 2{\cdot}235$, are shown in figures 9 (a) and (b). One of the major changes in the vertical velocity field is that the weak downward velocity cell near the centre of figure 8 (a) has shifted to the right, become much more intense, and has made a strong intrusion into the positive vertical velocity cross-roll pattern. A clearly defined tongue of negative temperature associated with this transient disturbance is seen in figure 9 (b). After this time, this negative velocity disturbance is observed to propagate in the $+y$ direction along the cross-roll pattern and then lose its identity. A second major change in the vertical velocity field seen in figure 9 (a) is the intense upward velocity centre which appears to have formed from the merging of two weaker cells on the roll-like feature located at $x \approx 2{\cdot}8$. This cell then propagates somewhat further in the $+y$ direction before weakening and losing its identity. Both

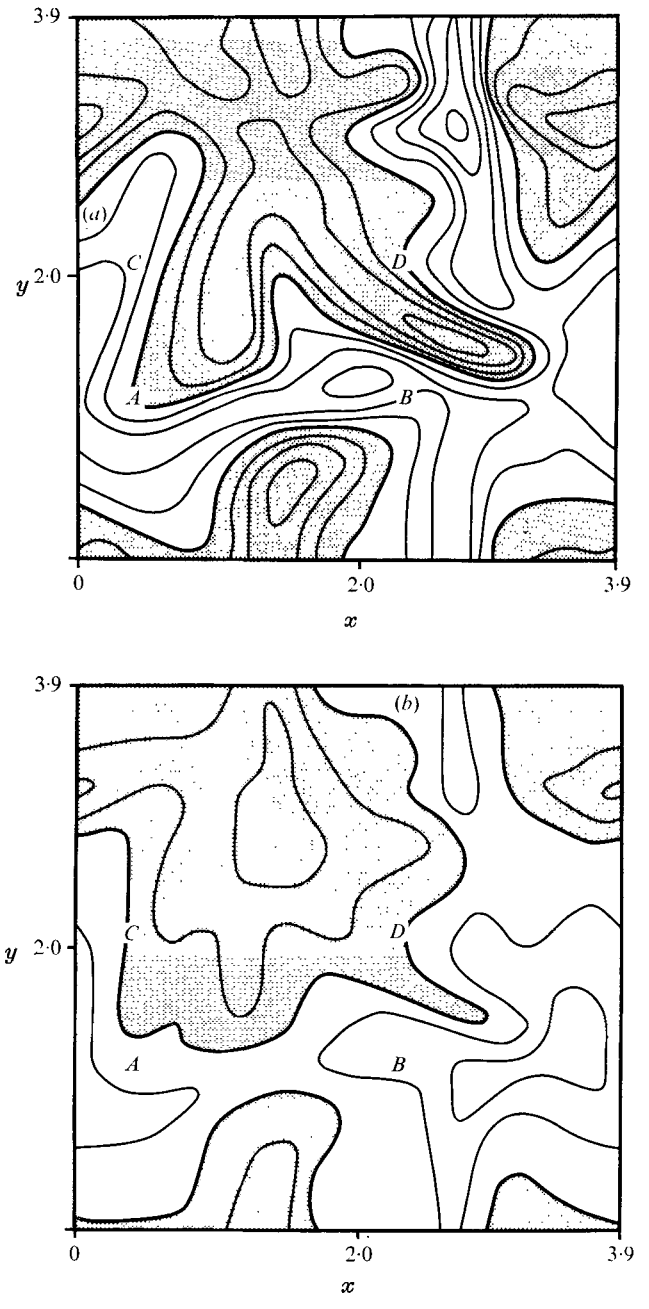

FIGURE 9. (*a*) Isotachs of vertical velocity w and (*b*) isotherms of temperature θ in the x, y plane at $Ra = 25\,000$. This figure is for $z = \frac{1}{2}$ at $t = 2{\cdot}235$. Notation is the same as in figure 8.

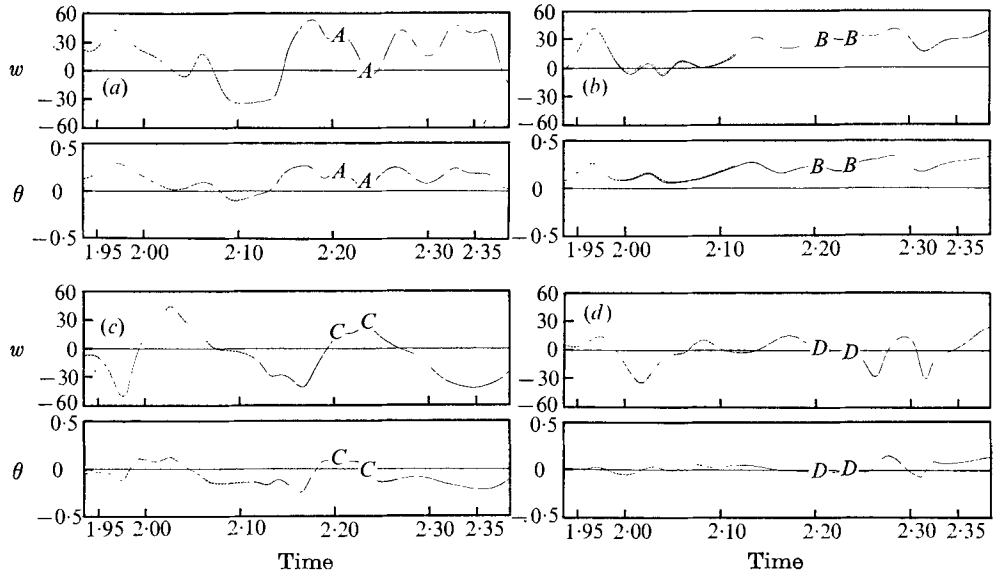

FIGURE 10. Time variation of w and θ on the mid-level $z = \frac{1}{2}$ for $Ra = 25\,000$ at the points denoted by (*a*) A, (*b*) B, (*c*) C and (*d*) D in figures 8 and 9. ——, results obtained from run E; – – –, time variation when the time step Δt was reduced by one-half (see appendix B).

of these disturbances appear to be examples of the type of short-lived waves observed by Willis & Deardorff (1970) for $Ra > 12\,000$. The present disturbances formed and dissipated in a time interval roughly given by $\tau \simeq 0{\cdot}10$.

The time dependence at the level $z = \frac{1}{2}$ is further examined by showing in figure 10 the time variations of w and θ at the four points denoted by A, B, C and D in figures 8 and 9. These time variations are shown for the time interval $1{\cdot}935 < t < 2{\cdot}385$, where the latter time is at the end of run E. The points labelled A, B, C or D in figure 10 indicate where these time plots intersect figures 8 and 9.

When the time variations at the four points are compared, it is seen that the type of oscillation is different at each point. This is one measure of the complexity of the time oscillations at $Ra = 25\,000$. Thus the simple picture of a mean roll pattern with the rolls parallel to the x axis is not valid for the present numerical simulation. As discussed above, the mean flow during the time variations shown in figure 10 appears to be more accurately described by a cross-roll pattern with upward velocity oriented along the lines $y \approx 1{\cdot}1$ and $x \approx 2{\cdot}8$.

The time variations seen in figure 10 can therefore be thought of as due to the superposition of finite amplitude disturbances upon the cross-roll mean flow pattern. The periods of the time oscillations in figure 10 are quite variable, being approximately in the range $0{\cdot}05 < \tau < 0{\cdot}20$. The mean flow itself is not steady but changes more slowly with time. As discussed previously, the cross-roll pattern apparently has the period $\tau \simeq 1{\cdot}3$.

In conclusion, the numerical periods obtained at $Ra = 9000$ and $Ra = 25\,000$ are compared with experimental and theoretical data. For $Ra = 9000$, the value $\tau \simeq 0{\cdot}28$ is found from figure 9 of Willis & Deardorff (1970). The same period is

also obtained from figure 12 of Clever & Busse (1974) for a wavelength $\lambda_x = 2{\cdot}1$. These results are in reasonable agreement with the period $\tau \simeq 0{\cdot}24$ found in run D at $Ra = 9000$. The range of values $0{\cdot}05 < \tau < 0{\cdot}20$ found in run E at $Ra = 25\,000$ is in qualitative agreement with the experimental data shown in figure 3 of Krishnamurti (1973) and with the theoretical results shown in figure 12 of Clever & Busse (1974).

The longer numerical periods, however, are not in agreement with either experimental or theoretical data. These periods are $\tau \simeq 0{\cdot}45$ for the large amplitude disturbances at $Ra = 9000$ and $\tau \simeq 1{\cdot}3$ for the mean flow at $Ra = 25\,000$. Longer period oscillations do exist in Bénard convection in air as indicated by Willis & Deardorff (1967). These experimental periods, however, are much longer than the above periods. The reason for this discrepancy may be that the numerically obtained periods are strongly influenced by the periodic side boundary conditions. Also Willis & Deardorff (1967) indicated that their long period oscillations may be strongly dependent on experimental conditions. They predicted that the short period oscillations would be more amenable to theoretical analysis.

6. The mean statistics for Bénard convection in air

In the present section we examine the mean properties of Bénard convection in air. These mean properties include the horizontal scale of the convection, the total kinetic energy K and the vertical heat flux Nu. In addition, a series of horizontally averaged statistics will be presented. These variables include the horizontally averaged temperature $\langle\theta\rangle$, the correlation of vertical velocity and temperature $r(w\theta)$, and the horizontally averaged kinetic energy $\langle k\rangle$. These quantities will be shown as functions of z for $Ra = 4000$, $Ra = 9000$ and $Ra = 25\,000$. The kinetic energy balance will also be discussed for these values of Ra. This discussion will follow that given by Deardorff & Willis (1967).

6.1. *The variation of horizontal scale with Ra*

In the present investigation two different types of horizontal scale are considered. The first is an integrated average scale S. For the vertical velocity field this average is given by

$$S_w = 2\pi\{w^2\}^{\frac{1}{2}}/\{-w\nabla_H^2 w\}^{\frac{1}{2}}, \tag{10}$$

where ∇_H^2 is the horizontal Laplacian operator and the brackets indicate that an average has been taken over the entire volume. An analogous scale S_θ is defined in terms of the temperature field. The second type of horizontal scale considered is the wavelength λ of the mean flow. It is this scale which corresponds to the roll wavelengths observed by Willis *et al.* (1972). However, the integrated average scales S_w and S_θ may be more relevant to the dynamics of the convection. This is particularly the case at $Ra = 9000$ and $Ra = 25\,000$, where large amplitude transient disturbances are superimposed on the mean flow.

Numerically calculated values of S_w, S_θ and λ_{num} are given in table 3 for runs A, B, D and E. For runs D and E the values given are the result of averaging the data over specified times during the calculations. In run D an average over six different times was used while in run E an average over ten different times was

taken. The values given for runs A and B represent the final steady-state values for these runs at $Ra = 4000$. Calculations were also performed with a two-dimensional numerical model at $Ra = 9000$ and $Ra = 25\,000$. These calculations are denoted in this table by run D–2D and run E–2D respectively. Owing to the two-dimensional constraint, these runs approached a steady state.

The data in table 3 indicate that S_w and S_θ are nearly the same as λ_{num} in runs A and B, where the convection is two-dimensional. For three-dimensional convection at $Ra = 9000$ and $Ra = 25\,000$, however, the scales S_w and S_θ are much smaller than λ_{num}. When the convection is constrained to be two-dimensional as in runs D–2D and E–2D, the values of S_w and S_θ are also smaller than λ_{num} but are not nearly as small as in runs D and E, with three-dimensional disturbances present. A comparison of S_w and S_θ in runs D and E indicates that S_w is the smaller and S_θ is the larger. This result is in conformity with the previous observations that the three-dimensional disturbances show up more strongly in the vertical velocity field than in the temperature field.

In table 3 it may be seen that the values of λ_{num} and λ_{exp} are in reasonable agreement for all cases except run E. In that case the mean flow did not take the form of rolls with $\lambda_y = 3{\cdot}9$ as expected. Instead the mean flow took the form of the cross-roll pattern discussed previously. This three-dimensional mean flow has the wavelength $\lambda = 2{\cdot}76$.

6.2. *The variation of K and Nu with Ra*

The calculated values of the total kinetic energy K and the mean vertical heat flux Nu are shown in the final two columns of table 3. It may be seen that the values of K and Nu for runs D and E are nearly the same as those calculated for runs D–2D and E–2D. Thus it appears that K and Nu are relatively insensitive measures of the dynamics of the convection. This is particularly the case for the heat flux Nu for the range of Ra considered. This may explain why Willis *et al.* (1972) were able to obtain good agreement between their experimental and numerical values of Nu for air. Their numerical calculations were carried out using a two-dimensional model for values of $Ra \leqslant 20\,000$.

The dependence of K and Nu on the disturbance wavelength λ_x was examined by making an additional calculation at $Ra = 9000$ with $s_x = 4{\cdot}90$ and $s_y = 3{\cdot}50$. This value of s_x allows the wavelength $\lambda_x = 2{\cdot}45$, which is essentially the observed value (Willis & Deardorff 1970). After some initial transients, the flow patterns were similar to those discussed previously for run D. The mean values $K = 138{\cdot}7$ and $Nu = 2{\cdot}24$ were obtained. Thus K and Nu changed relatively little as λ_x was increased from $\lambda_x = 2{\cdot}0$ (run D) to $\lambda_x = 2{\cdot}45$. This result and the data in tables 2 and 3 support the opinion of Clever & Busse (1974) that the onset of the oscillatory instability would have little effect upon Nu.

An estimate was made of the finite-difference truncation errors associated with Nu so that the present results could be compared with experimental and theoretical data. This was done by calculating Nu with higher resolution two-dimensional models and extrapolating the values to infinitely fine grid sizes (see Lipps & Somerville 1971). In this procedure it was assumed that the three-dimensional values of Nu change by the same amount on extrapolation as those

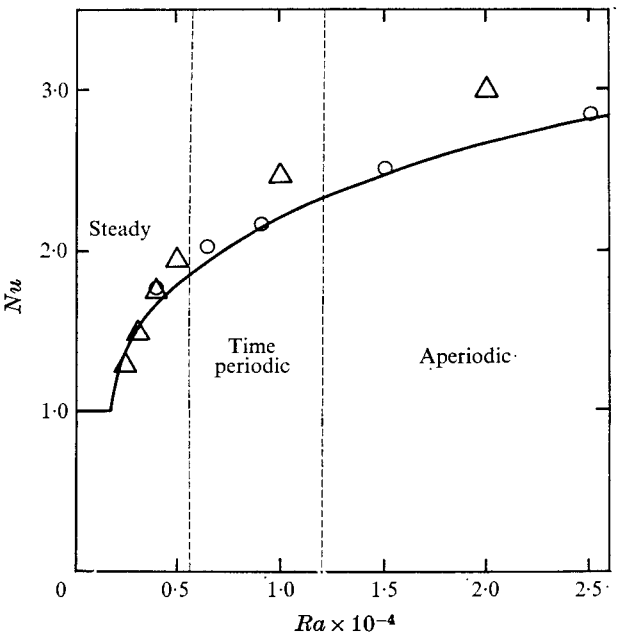

FIGURE 11. Heat transfer Nu as a function of Ra. ——, obtained from the data of Brown (1973); △, results from the analysis of Clever & Busse (1974), calculated for a roll wavelength of $\lambda = 2{\cdot}86$; ○, adjusted numerical values of Nu from the present study. The vertical dashed lines separate the three regimes of Bénard convection in air.

determined from the two-dimensional calculations. This assumption seems plausible since the values of Nu in table 3 are nearly independent of the dimensionality of the convection.

These adjusted values of Nu are indicated by the circles in figure 11. The solid line represents the experimental data of Brown (1973). The average value obtained from runs A and B was used for the circle at $Ra = 4000$. The circles at $Ra = 6500$, 9000 and 25 000 were obtained from runs $F1$, D and E respectively. Finally, the circle at $Ra = 15\,000$ represents calculations from a run with the same grid dimensions N_x, N_y and N_z as run D, horizontal aspect ratios $s_x = 4{\cdot}18$ and $s_y = 3{\cdot}71$ and a total simulated time of $T = 3{\cdot}75$.

The triangles in this figure represent values of Nu calculated by Clever & Busse (1974) for a roll wavelength of $\lambda = 2{\cdot}86$. The value at $Ra = 4000$ was obtained by graphical interpolation; the other values of Nu were taken directly from table 1 of their study. It is seen that their value and the present value of Nu are in excellent agreement at $Ra = 4000$. For the observed values of λ, it is well known that an increase in λ at a fixed Ra gives a decrease in Nu (Lipps & Somerville 1971). Thus, where the observed wavelengths are shorter than $\lambda = 2{\cdot}86$ at small Ra, the values of Nu calculated by Clever & Busse are smaller than the observed values. At large Ra, where the observed wavelengths are longer than $\lambda = 2{\cdot}86$, the calculated values of Nu are larger than the observed values.

The circles in figure 11 indicate that the numerical values of Nu given for $Ra = 9000$, $Ra = 15\,000$ and $Ra = 25\,000$ fall within the region of uncertainty of

Run	Ra	S_w	S_θ	λ_{num}	λ_{exp}	K	Nu
A	4 000	2·96	2·98	3·00	2·8	38·4	1·75
B	4 000	2·48	2·50	2·52	2·8	45·5	1·88
D	9 000	1·89	2·60	3·50	3·6	134·3	2·22
D–2D	9 000	3·27	3·28	3·50	3·6	135·1	2·25
E	25 000	1·34	1·99	2·76	4·0	482·3	2·94
E–2D	25 000	3·14	3·10	3·90	4·0	503·4	2·89

TABLE 3. Values of the length scales S_w and S_θ, the wavelengths λ_{num} and λ_{exp}, and K and Nu. Values of λ_{exp} were taken from Willis *et al.* (1972).

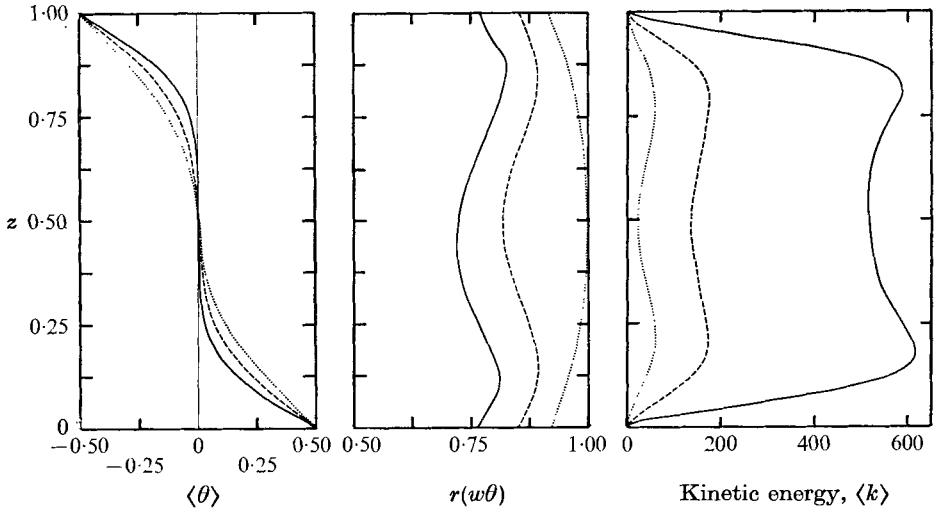

FIGURE 12. Vertical variations of $\langle\theta\rangle$, $r(w\theta)$ and $\langle k\rangle$ for three Rayleigh numbers. ·····, Ra = 4000; ------, Ra = 9000; ——, Ra = 25 000.

the experimental data. However, the numerical values of Nu for Ra = 4000 and Ra = 6500 appear to be too large. One possible reason for this discrepancy is that the experimental convection is only quasi-two-dimensional at low Ra. This tendency is clearly seen in the photographs of Willis *et al.* (1972) for convection in air at Ra = 4000 and Ra = 6200. In the numerical calculations at Ra = 4000 the final steady states are strictly two-dimensional. In run A the values of Nu were lower by about 0·07 just before the flow started evolving towards the final roll pattern. With this reduction in Nu included, the circle at Ra = 4000 would be in much better agreement with the experimental data.

6.3. *The variation of horizontally averaged statistics with Ra*

In figure 12 some horizontally averaged statistics of the convection are shown as functions of z for Ra = 4000, Ra = 9000 and Ra = 25 000. The variables plotted are the horizontally averaged temperature $\langle\theta\rangle$, the correlation of vertical velocity and temperature $r(w\theta)$, and the horizontally averaged kinetic energy $\langle k\rangle$. In the present notation $k(x, y, z, t)$ represents the spatial and temporal distribution of kinetic energy and $\langle k\rangle$ is its horizontal average. The data for Ra = 4000

were obtained from the steady-state values at the end of run A. The data for the larger values of Ra represent time averages as was discussed for table 3.

The three curves for $\langle\theta\rangle$ in figure 12 show the typical formation of the isothermal temperature gradient near $z = \frac{1}{2}$ as Ra is increased. There is no reverse temperature gradient for $Ra = 9000$ or $Ra = 25\,000$. It is of interest to note that the two-dimensional runs D–2D and E–2D do give a reverse temperature gradient near $z = \frac{1}{2}$. Thus the three-dimensionality in the present calculations acts in some way to prevent the formation of the reverse temperature gradient.

The data in figure 12 for $r(w\theta)$ indicate that w and θ are highly correlated for $Ra = 4000$. The value of $r(w\theta)$ is almost exactly one at $z = \frac{1}{2}$. When three-dimensional motions develop, the values of $r(w\theta)$ are reduced and the largest values are at the top of the boundary layers rather than at $z = \frac{1}{2}$. These properties of $r(w\theta)$ are consistent with the observed form of three-dimensional disturbances at $Ra = 6500$, which are discussed in appendix A. For $Ra = 25\,000$ a vertical asymmetry exists in $r(w\theta)$. This vertical asymmetry and that of other data at $Ra = 25\,000$ are almost certainly due to lack of representativeness in the time averaging (only ten times were averaged) rather than to anything in the dynamics.

The curves for $\langle k\rangle$ in figure 12 show that the magnitude of $\langle k\rangle$ increases rapidly as Ra is increased. Equally important, however, is the change in shape of the kinetic energy variation when three-dimensional motions are present. For $Ra = 4000$ the maxima in $\langle k\rangle$ at $z = 0{\cdot}22$ and $z = 0{\cdot}78$ are more than twice the magnitude of the minimum in $\langle k\rangle$ at $z = \frac{1}{2}$. When the convection is three-dimensional the two maxima in $\langle k\rangle$ are still present, but the relative variation of $\langle k\rangle$ in the central region of the fluid is much less.

The present data clearly indicate that the change in the variation with height of $r(w\theta)$ and $\langle k\rangle$ is due to three-dimensionality and not due to simply increasing the Rayleigh number. Data for $r(w\theta)$ and $\langle k\rangle$ were obtained for runs D–2D and E–2D, where the flow was constrained to be two-dimensional. For $r(w\theta)$ the two-dimensional values are larger and a single maximum occurs at $z = \frac{1}{2}$. For example, the E–2D results for $Ra = 25\,000$ give a maximum value for $r(w\theta)$ of 0·96 at $z = \frac{1}{2}$ and a vertical mean value of 0·90. For $Ra = 9000$ the D–2D results give a maximum value of 0·99 and a vertical mean value of 0·94. When the vertical variation of $\langle k\rangle$ for two-dimensional runs is considered, it is found that at both $Ra = 9000$ and $Ra = 25\,000$ the maxima in $\langle k\rangle$ are more than double the minimum value at $z = \frac{1}{2}$. Thus the two-dimensional results from runs D–2D and E–2D appear to have more in common with run A at $Ra = 4000$ than with their three-dimensional counterparts, runs D and E.

6.4. *The kinetic energy balance*

If we take the scalar product of **V** with the momentum equation (3) and average over the horizontal domain, the following equation for the kinetic energy balance is obtained:

$$\frac{\partial}{\partial t}\langle k\rangle = Pr\,Ra\,\langle w\theta\rangle - \frac{\partial}{\partial z}\langle w(k+p)\rangle - Pr\left\langle \frac{\partial u_i}{\partial x_j}\frac{\partial u_i}{\partial x_j}\right\rangle + Pr\frac{\partial^2}{\partial z^2}\langle k\rangle \quad (i = 1, 2, 3;\ j = 1, 2, 3). \tag{11}$$

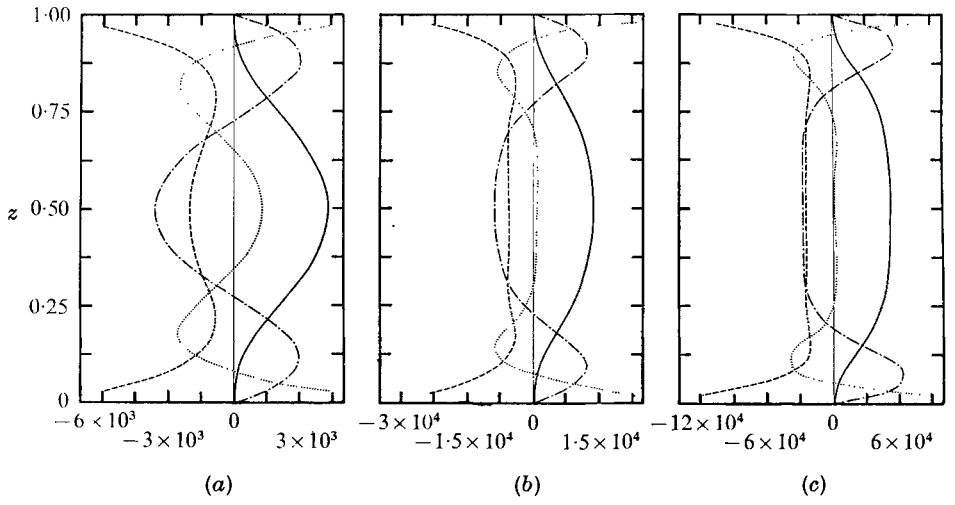

FIGURE 13. Vertical variation of terms in the horizontally averaged kinetic energy equation for (*a*) $Ra = 4000$, (*b*) $Ra = 9000$ and (*c*) $Ra = 25\,000$. ——, production, $Pr\,Ra\langle w\theta\rangle$; ------, dissipation, $-Pr\langle(\partial u_i/\partial x_j)(\partial u_i/\partial x_j)\rangle$; ·····, molecular transfer, $Pr\,\partial^2\langle k\rangle/\partial z^2$; –·–·–·–, diffusion, $-\partial\langle w(k+p)\rangle/\partial z$.

This equation is equivalent to equation (15) of Deardorff & Willis (1967). Following their discussion the four terms on the right side of this equation will be denoted respectively by production, diffusion, dissipation and molecular transfer of kinetic energy. These four terms were calculated as functions of z for $Ra = 4000$, $Ra = 9000$ and $Ra = 25\,000$. The results at the two larger values of Ra represent time averages as for previous data. At $Ra = 4000$ the results were obtained from the end of run *A*.

Figure 13 shows the kinetic energy balance for the three values of Ra. At $Ra = 4000$ the curves appear typical of low Rayleigh number convection with broad boundary layers and sinusoidal-type variations in the interior. For $Ra = 9000$ and $Ra = 25\,000$ the curves have a flat appearance in the interior and the boundary layers are thinner. This is more characteristic of high Rayleigh number convection.

The kinetic energy balance was examined by Deardorff & Willis (1967) at $Ra = 6{\cdot}3 \times 10^5$, $Ra = 2{\cdot}5 \times 10^6$ and $Ra = 1{\cdot}0 \times 10^7$. The present curves at $Ra = 25\,000$ have broader boundary layers and the boundary-layer maxima are not as sharp, but in other respects the present data are very similar to their data for much larger values of Ra. This similarity includes the following features.

(i) The production has a broad maximum in the interior of the fluid.

(ii) The dissipation is strongly negative near the boundaries, has a minimum magnitude at the top of the boundary layers and is constant near $z = \frac{1}{2}$.

(iii) The diffusion has a well-defined maximum in the boundary layers and approaches a negative constant value in the interior. When comparing the negative values of diffusion and dissipation in the interior, it may be seen that the relative magnitude of the dissipation becomes larger as Ra is increased. The same trend is seen in the data of Deardorff & Willis.

(iv) The curve of molecular transfer changes sign near the boundaries, has well-defined minima in the boundary layers and has two weak maxima just outside the boundary layers.

7. Summary and conclusions

Three-dimensional numerical solutions at $Ra = 4000$ produced steady two-dimensional convection with the roll wavelengths of $\lambda_{\text{num}} = 3{\cdot}00$ in run A and $\lambda_{\text{num}} = 2{\cdot}52$ in run B. These values are in good agreement with the experimental data. Willis *et al.* (1972) found the mean wavelength $\lambda_{\text{exp}} = 2{\cdot}8$. As indicated by Lipps & Somerville (1971), initial-value calculations using a two-dimensional numerical model will predict roll wavelengths shorter than those observed in experiments.

Finite amplitude travelling wave disturbances developed in run C at $Ra = 6500$ with the wavelength $\lambda_x = 2{\cdot}0$. The most unstable wavelength from the linear analysis of Clever & Busse (1974) is $\lambda_x = 2{\cdot}6$. The present value of λ_x is strongly influenced by the choice of the horizontal aspect ratio $s_x = 4{\cdot}00$. The dynamics of the $\lambda_x = 2{\cdot}0$ disturbances was examined in detail. When these disturbances were small amplitude standing waves, the period was $\tau = 0{\cdot}24$. When they became finite amplitude travelling waves, the period was $\tau = 0{\cdot}27$. The values of K, Nu, $\{PK\}$ and P changed relatively little owing to the presence of time-periodic disturbances.

The numerical period $\tau = 0{\cdot}24$ is in good agreement with the period $\tau = 0{\cdot}23$ obtained from Clever & Busse (1974). The finite amplitude period $\tau = 0{\cdot}27$ compares reasonably well with the experimental period $\tau \simeq 0{\cdot}32$ found from Willis & Deardorff (1970). The variation of the numerical τ as the disturbances reach finite amplitude is in good agreement with the conclusion of Busse & Whitehead (1974) that the period is proportional to the circulation time of the mean flow.

In appendix A the total flow at $Ra = 6500$ is separated into the mean flow (average taken along x) and the disturbance flow. Cross-sections are shown for the mean two-dimensional rolls $(\overline{\mathbf{V}}, \overline{\theta})$ and for the three-dimensional disturbance fields $(\mathbf{V}', \theta')$. The energy balance between the mean flow kinetic energy $\overline{K}$, the disturbance kinetic energy K' and the available potential energy P is calculated. The transformations $\{PK'\}$ and $\{\overline{K}K'\}$ are both positive, $\{PK'\}$ being nearly twice the magnitude of $\{\overline{K}K'\}$.

When K' is separated into the components K'_u, K'_v and K'_w the present analysis indicates that $\{PK'\}$ is the energy source maintaining K'_w and K'_u against dissipation. The K'_v kinetic energy is maintained against dissipation by the $C_3 + C_4$ component of the total $\{\overline{K}K'\}$ transformation. The large amplitude v' oscillations near $z = \frac{1}{2}$ are maintained owing to the vertical advection of $\overline{v}$ momentum by the w' oscillations. The gradient $\partial v'/\partial x$ provides the major contribution to the vertical component of the disturbance vorticity ζ'. According to the theories of Busse (1972) and Clever & Busse (1974), the oscillatory nature of the disturbances is associated with the existence of ζ'.

The travelling wave disturbances at $Ra = 9000$ took on a more complex form. The weaker disturbances on the centre roll had the period $\tau \simeq 0{\cdot}24$ whereas the

much larger disturbances on the outside roll had the period $\tau \simeq 0{\cdot}45$. New forms of disturbances appeared at $Ra = 25\,000$. These were apparently similar to the breaking waves and isolated sharp-crested waves of short wavelength seen by Willis & Deardorff (1970). In the present numerical solution at $Ra = 25\,000$, the mean flow took the form of a semi-cross-roll pattern. The mean flow was not constant, but had a period given by $\tau \simeq 1{\cdot}3$. Disturbances superimposed upon the mean flow had a broad range of periods given approximately by $0{\cdot}05 < \tau < 0{\cdot}20$.

The short period fluctuations found at $Ra = 9000$ and $Ra = 25\,000$ are in reasonable agreement with experimental and theoretical data. The period $\tau \simeq 0{\cdot}28$ at $Ra = 9000$ is obtained from both Willis & Deardorff (1970) and Clever & Busse (1974). This value corresponds to the period $\tau \simeq 0{\cdot}24$ found in run *D*. The range $0{\cdot}05 < \tau < 0{\cdot}20$ found in run *E* at $Ra = 25\,000$ is in qualitative agreement with the experimental data shown in Krishnamurti (1973) and with the theoretical calculations of Clever & Busse (1974).

The longer numerical periods, however, are not in agreement with either experimental or theoretical data. The periods $\tau \simeq 0{\cdot}45$ for the large amplitude disturbances at $Ra = 9000$ and $\tau \simeq 1{\cdot}3$ for the mean flow at $Ra = 25\,000$ may be strongly influenced by the finite horizontal domain and the periodic side boundary conditions. The periods of the longer period oscillations that do exist in air (Willis & Deardorff 1967) are much longer than the above periods.

The long period fluctuations in air at low Ra may represent deviations of the flow patterns from strict two-dimensionality (Willis & Deardorff 1970). In the present calculations at $Ra = 4000$ the flow is strictly two-dimensional and the long period fluctuations do not exist. It is apparently the strict two-dimensionality in the mean flow at $Ra = 4000$ and $Ra = 6500$ that is responsible for the numerical values of Nu being slightly larger than the experimental ones (Brown 1973). The numerical values of Nu at $Ra = 9000$, 15 000 and 25 000 are in good agreement with the experimental values (see figure 11).

In § 6 several comparisons are made between two- and three-dimensional convection at $Ra = 9000$ and $Ra = 25\,000$. The horizontal scales S_w and S_θ are much smaller when three-dimensional motions are present; however, the values of the kinetic energy K and the heat transfer Nu are relatively unchanged. No reverse mean temperature gradient exists at $z = \frac{1}{2}$ when the flow is three-dimensional whereas a reverse temperature gradient does exist for two-dimensional flow. Three-dimensionality decreases the magnitude of the correlation $r(w\theta)$ and gives rise to a pair of maxima at the tops of the boundary layers instead of one maximum at $z = \frac{1}{2}$. When the vertical variation of the kinetic energy $\langle k \rangle$ is considered, three-dimensionality significantly reduces the relative difference in magnitude between the maxima at the top of the boundary layers and the minimum at $z = \frac{1}{2}$.

The kinetic energy balance is calculated for $Ra = 4000$, 9000 and 25 000 in §6.4. The various quantities calculated as a function of z are the production, diffusion, dissipation and molecular transfer of kinetic energy. When the present data for the kinetic energy balance at $Ra = 25\,000$ are compared with the data of Deardorff & Willis (1967) at much larger values of Ra, there is significant agreement. The same is also true when the variation with height of $\langle \theta \rangle$, $r(w\theta)$ and $\langle k \rangle$

at $Ra = 25\,000$ is compared with their data. These results suggest that the most important dynamics associated with highly turbulent convection in air are already present at $Ra = 25\,000$.

I wish to express my thanks to John B. Robinson, who gave invaluable aid in programming and analysis of the data. Richard C. J. Somerville and Gareth P. Williams read the manuscript and made many helpful suggestions. The author has also benefited from correspondence with Friedrich H. Busse. The calculations were carried out on a UNIVAC/1108. The figures were drafted by Philip G. Tunison and staff, and the manuscript typed by Betty M. Williams.

Appendix A. Detailed energetics and synoptics at $Ra = 6500$

The total flow field is separated into a mean component and a disturbance component. The mean is taken with respect to the x axis:

$$\mathbf{V}(x,y,z,t) = \overline{\mathbf{V}}(y,z,t) + \mathbf{V}'(x,y,z,t), \tag{A 1}$$

$$\theta(x,y,z,t) = \overline{\theta}(y,z,t) + \theta'(x,y,z,t). \tag{A 2}$$

The mean flow $(\overline{\mathbf{V}}, \overline{\theta})$ takes the form of two-dimensional rolls while the disturbance flow $(\mathbf{V}', \theta')$ represents the three-dimensional disturbances superimposed upon the rolls.

A 1. *The detailed energy equations*

The mean kinetic energy $\overline{K}$ and the disturbance energy K' are defined by

$$\overline{K} = \frac{1}{2}\int_0^1 \langle \overline{u}^2 + \overline{v}^2 + \overline{w}^2 \rangle \, dz, \tag{A 3}$$

$$K' = \frac{1}{2}\int_0^1 \langle u'^2 + v'^2 + w'^2 \rangle \, dz. \tag{A 4}$$

The sum of $\overline{K}$ and K' is K, the total kinetic energy. Since the available potential energy P is defined according to (5 *b*), it is evident that $P' \equiv 0$, so that $\overline{P} \equiv P$. The equations for the time rates of change of $\overline{K}$, K' and P are

$$d\overline{K}/dt = -\{\overline{K}K'\} + \{P\overline{K}\} - \overline{D}, \tag{A 5}$$

$$dK'/dt = \{\overline{K}K'\} + \{PK'\} - D', \tag{A 6}$$

$$dP/dt = -\{P\overline{K}\} - \{PK'\} + PP, \tag{A 7}$$

where the transformations $\{P\overline{K}\}$, $\{PK'\}$ and $\{\overline{K}K'\}$ are defined by

$$\{P\overline{K}\} = Pr\, Ra \int_0^1 \langle \overline{w}\overline{\theta} \rangle \, dz, \tag{A 8}$$

$$\{PK'\} = Pr\, Ra \int_0^1 \langle w'\theta' \rangle \, dz, \tag{A 9}$$

$$\{\overline{K}K'\} = C_1 + C_2 + C_3 + C_4 + C_5 + C_6, \tag{A 10}$$

where $C_1, \ldots, C_6$ are given by

$$C_1 = -\int_0^1 \left\langle u'v' \frac{\partial \bar{u}}{\partial y} \right\rangle dz, \quad C_2 = -\int_0^1 \left\langle u'w' \frac{\partial \bar{u}}{\partial z} \right\rangle dz,$$

$$C_3 = -\int_0^1 \left\langle v'^2 \frac{\partial \bar{v}}{\partial y} \right\rangle dz, \quad C_4 = -\int_0^1 \left\langle v'w' \frac{\partial \bar{v}}{\partial z} \right\rangle dz,$$

$$C_5 = -\int_0^1 \left\langle v'w' \frac{\partial \bar{w}}{\partial y} \right\rangle dz, \quad C_6 = -\int_0^1 \left\langle w'^2 \frac{\partial \bar{w}}{\partial z} \right\rangle dz.$$

The transformations $\{P\bar{K}\}$ and $\{PK'\}$ represent the mean and disturbance components of the total $\{PK\}$ transformation. The $\{\bar{K}K'\}$ transformation represents the conversion of basic kinetic energy into disturbance kinetic energy. The dissipation rates $\bar{D}$ and D' are as given in (6 *d*) with the velocity components $\bar{\mathbf{V}}$ and $\mathbf{V}'$ used in $\bar{D}$ and D' respectively.

Equation (A 6) for the time rate of change of K' can be separated into the three component equations

$$\frac{dK'_u}{dt} = \int_0^1 \left\langle p' \frac{\partial u'}{\partial x} \right\rangle dz + C_1 + C_2 - D'_u, \tag{A 11}$$

$$\frac{dK'_v}{dt} \int_0^1 = \left\langle p' \frac{\partial v'}{\partial y} \right\rangle dz + C_3 + C_4 - D'_v \tag{A 12}$$

$$\frac{dK'_w}{dt} = \int_0^1 \left\langle p' \frac{\partial w'}{\partial z} \right\rangle dz + C_5 + C_6 + \{PK'\} - D'_w, \tag{A 13}$$

where K'_u, K'_v, K'_w and D'_u, D'_v, D'_w are the kinetic energies and dissipation rates associated with the velocity components u', v' and w' respectively. Note that the three pressure-work integrals must sum to zero since the disturbance's divergence must vanish.

A 2. *Detailed energetics and flow patterns at Ra = 6500*

The energy budgets for $\bar{K}$, K' and P are indicated respectively by (A 5)–(A 7). At the end of run *F*1, the energetics with respect to the total K, P and $\{PK\}$ were in a steady state, however there was still some transfer of energy from $\bar{K}$ to K' at this time. The magnitude of this energy exchange was decreasing with time and an extrapolation procedure was used to estimate the steady-state energetics appropriate to (A 5)–(A 7). The magnitude of this extrapolation was never more than 2·5 %.

The energy balance for the extrapolated steady state is shown in figure 14. This three-box diagram indicates that K' receives energy through both the $\{PK'\}$ and the $\{\bar{K}K'\}$ transformations. The $\{PK'\}$ transformation is the larger, accounting for 62 % of the total conversion into K' kinetic energy. The remaining 38 % is accounted for by the $\{\bar{K}K'\}$ transformation. The values of the six terms $C_1, \ldots, C_6$, which make up the total $\{\bar{K}K\}$ transformation, are given in table 4. The present energy balance has been calculated for $\lambda_x = 2{\cdot}0$. As indicated in § 4.1, the most unstable wavelength obtained from the linear theory of Clever & Busse (1974) is $\lambda_x = 2{\cdot}6$. Although the detailed values shown in figure 14 will

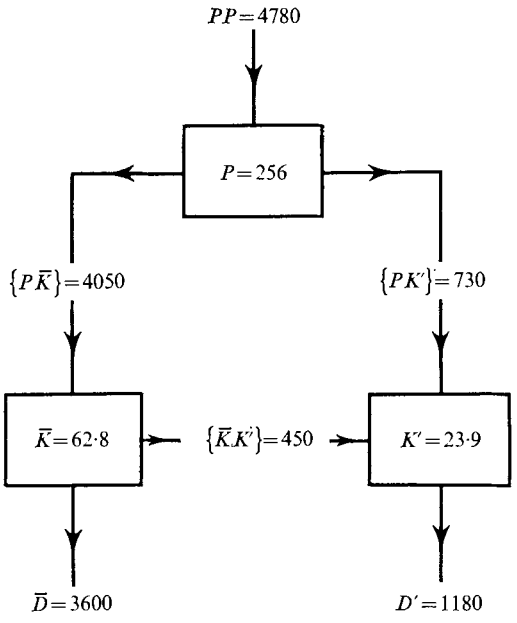

FIGURE 14. Three-box energy diagram for $Ra = 6500$. These data are the extrapolated values obtained from run $F1$. The various transformations and the different forms of energy are discussed in §A 1.

change with λ_x, it is thought that the qualitative features of this figure will remain unchanged.

The energetics can be better understood after an examination of the mean flow and the disturbance flow at the end of run $F1$. The mean flow fields $\overline{u}$, $\overline{v}$, $\overline{w}$ and $\overline{\theta}$ are shown in figure 15. These patterns for $\overline{v}$, $\overline{w}$ and $\overline{\theta}$ in the y, z plane indicate a typical two-dimensional roll structure. The $\overline{u}$ field has a maximum value of 0·6 compared with maximum amplitudes of 18·7 and 12·9 for the $\overline{v}$ and $\overline{w}$ velocities, respectively. Since the sum $C_1 + C_2$ is negative, implying very weak transformation of disturbance kinetic energy into $\overline{u}$ kinetic energy, the $\overline{u}$ field is generated by the disturbances. Dynamically it is of negligible importance since it is very weak.

The disturbance flow fields u, v', w' and θ' in the x, z plane are shown in figure 16. These cross-sections are for $y = \frac{1}{2}s_y$, so that they intersect the axis of the mean flow rolls at $z = \frac{1}{2}$. Along this axis, where $\overline{v}$ and $\overline{w} = 0$, the disturbance velocities v' and w' are at or near their maximum amplitudes. The disturbance flow patterns move from left to right without change of shape. Thus they have a positive phase velocity c_x.

The fields shown in figure 16 indicate that the θ' oscillations lead the w' oscillations by about 54° at $z = \frac{1}{2}$. Near the boundaries, where θ' is larger, the w' and θ' oscillations are nearly in phase. These results give rise to the positive $\{PK'\}$ transformation. They also indicate that the correlation function $r(w'\theta')$ should have a maximum value in the boundary layers and a minimum at $z = \frac{1}{2}$. This is the behaviour of the correlation $r(w\theta)$ for the total w and θ when the disturbances are of large amplitude at $Ra = 9000$ and $Ra = 25\,000$ (see figure 12).

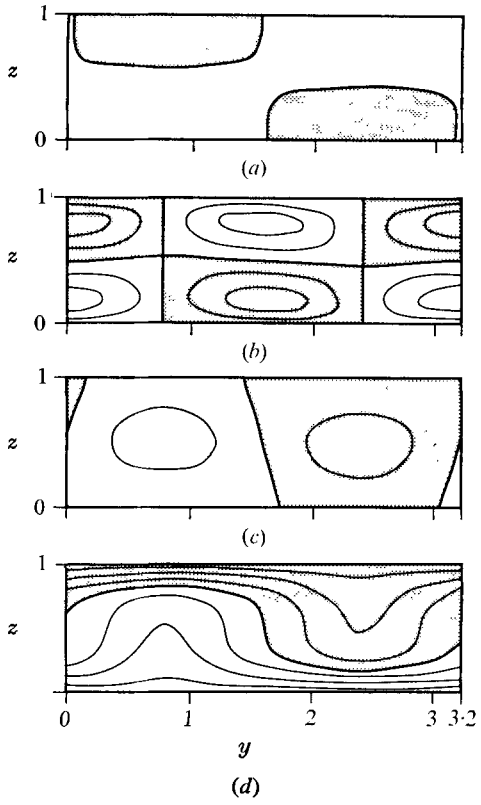

FIGURE 15. The mean flow in the y, z plane for $Ra = 6500$. These cross-sections are for the end of run $F1$. (*a*) $\bar{u}$ velocity. (*b*) $\bar{v}$ velocity. (*c*) $\bar{w}$ velocity. (*d*) θ temperature. The contour interval for the velocities is 7·5 and for the temperature is 0·15. Stippled areas are negative.

	u'	v'	w'	Total
Kinetic energy	$K'_u = 4{\cdot}4$	$K'_v = 12{\cdot}4$	$K'_w = 7{\cdot}1$	$K' = 23{\cdot}9$
$\{\bar{K}K'\}$	$C_1 = -4$	$C_3 = -37$	$C_5 = -163$	$K\{\bar{K}'\} = 450$
	$C_2 = 2$	$C_4 = 581$	$C_6 = 71$	
$\{PK'\}$	—	—	$\{PK'\} = 730$	$\{PK'\} = 730$
Dissipation	$D'_u = 365$	$D'_v = 542$	$D'_w = 273$	$D' = 1180$
Pressure-work	$PW_x = 367$	$PW_y = -2$	$PW_z = -365$	$PW_{\text{tot}} = 0$

TABLE 4. The detailed energetics associated with u', v' and w' at $Ra = 6500$. In each column the terms given correspond to the terms shown in (A 11), (A 12), (A 13) and (A 6) respectively. These values are for the asymptotic steady state.

The disturbance flow in the y, z plane is shown in figure 17. These cross-sections are given for the value of x indicated by the arrow in figure 16. This value of x was chosen such that the fields of v' and w' would be near their maximum amplitudes. The field of u' is therefore not near its maximum amplitude; however, the basic variation of u' with y is revealed in this figure. A comparison of figures 15 and 17 confirms that the maximum amplitudes of v' and w' are at or near the mean roll

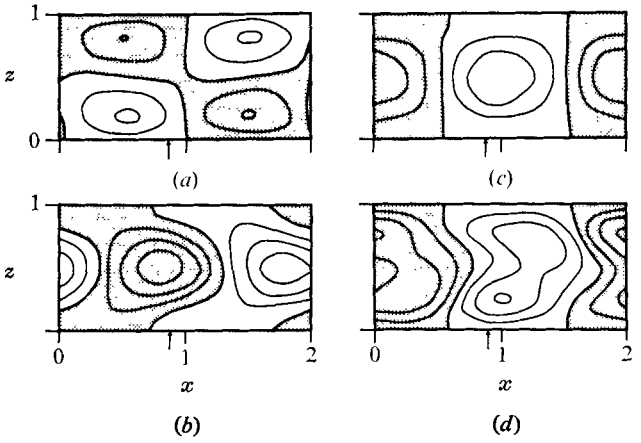

FIGURE 16. Fields of (*a*) u', (*b*) v', (*c*) w' and (*d*) θ' in the x, z plane. These cross-sections are for $y = \frac{1}{2}s_y$. Stippled areas are negative. The contour interval for the velocities is 3·75 and for the temperature is 0·04.

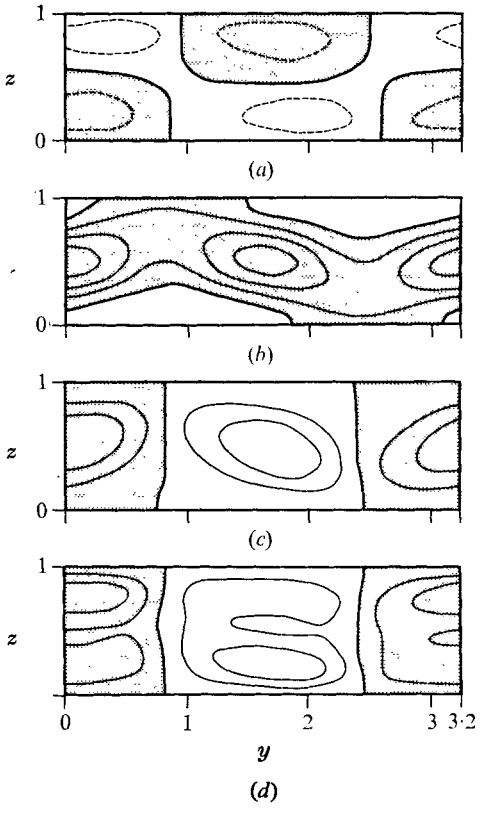

FIGURE 17. Fields of (*a*) u', (*b*) v', (*c*) w' and (*d*) θ' in the y, z plane. These cross-sections are for the value of x indicated by the arrow in figure 16. Stippled areas are negative. Solid contours are the same as in figure 16. The broken lines in the u' cross-section represent 1·875 contours.

axis. Figure 17 also shows that v' has one sign in y and a wavenumber $n_y = 2$ variation near $z = \frac{1}{2}$. Near the boundaries, however, v' has a wavenumber $n_y = 1$ variation and does change sign.

Detailed discussion of K'. The equations for the separate components K'_u, K'_v and K'_w of the K' kinetic energy are given by (A 11)–(A 13). The steady-state values of the terms in each of these equations are given in table 4. The pressure-work terms were not calculated directly, but were obtained from the sum of the other terms in each equation. The time derivatives of K'_u, K'_v and K'_w are assumed to vanish in the asymptotic steady state.

The data in table 4 show that the $\{PK'\}$ transformation is the positive energy source term for K'_w. Since $C_5 + C_6 = -92$, this component of the total $\{\bar{K}K'\}$ transformation represents a small energy sink. The excess net energy from this source not balanced by the dissipation D'_w is transferred into the K'_u and K'_v energy components through the pressure-work term PW_z. The K'_u energy is the apparent recipient of this energy through the positive PW_x. This pressure-work term almost exactly balances the dissipation D'_u. In the K'_v energy equation (A 12), the sum $C_3 + C_4$ is the source term, which almost exactly balances the dissipation D'_v. The importance of this source term is evident since K'_v is greater than the sum of K'_u and K'_w.

At the level $z = \frac{1}{2}$ the v' oscillations have their largest amplitude along the mean roll axis, where both $\partial\bar{v}/\partial z$ and w' have a large amplitude. Thus near this level, where the v' kinetic energy is largest, the primary source of energy is evidently associated with the vertical advection of $\bar{v}$ momentum by the w' oscillations. This positive energy source is represented by C_4, which is the largest of the components of the $\{\bar{K}K'\}$ transformation. The data shown in figures 15 and 17 indicate that as w' changes sign from one mean flow roll to the next, so also does the gradient $\partial\bar{v}/\partial z$, thus allowing v' to maintain one sign in y. This line of reasoning also explains the $n_y = 2$ wavenumber variation in v' near $z = \frac{1}{2}$.

The dynamics of the v' oscillations appears to be different near the boundaries. The $n_y = 1$ wavenumber variation in v' shown in figure 17 is approximately 90° out of phase with w'. The correlation of $\partial u'/\partial x$ and $\partial v'/\partial y$ has been calculated as a function of z. This correlation has values close to 0·90 in the boundary layers and is near $-1{\cdot}0$ at $z = \frac{1}{2}$. Thus near the boundaries $\partial u'/\partial x$ and $\partial v'/\partial v$ are almost in phase and together supply the convergence required by continuity to maintain the w' oscillations. Since the energy source for K'_w is the $\{PK'\}$ transformation, it would appear that $\{PK'\}$ is the indirect energy source for the boundary-layer v' oscillations.

The final topic of discussion is the vertical component of the disturbance vorticity ζ'. According to the theories of Busse (1972) and Clever & Busse (1974), the oscillatory behaviour of the disturbances is associated with ζ'. In the present calculations, the main contribution to ζ' is through the gradient $\partial v'/\partial x$. As seen in figures 16 and 17, this gradient has maximum amplitude near $z = \frac{1}{2}$, so that ζ' is largest there also. The above discussion for the v' oscillations indicates that the primary energy source associated with ζ' is the C_4 component of the total $\{\bar{K}K'\}$ transformation.

Appendix B. A discussion of time and space truncation errors

The primary topic of this appendix is the time truncation error associated with the DuFort–Frankel difference scheme. This scheme is used to represent the finite-difference forms of the viscous and diffusive terms in (3) and (4). If the limit $\Delta z \to 0$ is taken for the finite-difference equations, but the ratios $\Delta x/\Delta z$, $\Delta y/\Delta z$ and $\Delta t/\Delta z$ are held constant in this limit, then the resulting continuous equations will contain artificial second time derivatives (Richtmyer & Morton 1967, p. 177):

$$\frac{\partial \mathbf{V}}{\partial t}+\frac{\partial}{\partial x}(u\mathbf{V})+\frac{\partial}{\partial y}(v\mathbf{V})+\frac{\partial}{\partial z}(w\mathbf{V}) = -\nabla p + Pr\,Ra\,\theta\mathbf{k}+Pr\left(\nabla^2\mathbf{V}-\beta\frac{\partial^2\mathbf{V}}{\partial t^2}\right), \quad \text{(B 1)}$$

$$\frac{\partial \theta}{\partial t}+\frac{\partial}{\partial x}(u\theta)+\frac{\partial}{\partial y}(v\theta)+\frac{\partial}{\partial z}(w\theta) = \nabla^2\theta-\beta\frac{\partial^2\theta}{\partial t^2}, \quad \text{(B 2)}$$

where

$$\beta = \left(\frac{\Delta t}{\Delta z}\right)^2\left\{1+\left(\frac{\Delta z}{\Delta x}\right)^2+\left(\frac{\Delta z}{\Delta y}\right)^2\right\}. \quad \text{(B 3)}$$

Thus, for finite values of β, the finite-difference equations with the DuFort–Frankel scheme will represent approximate solutions to (B 1) and (B 2) instead of (3) and (4).

If $\mathbf{V}$ and θ have the time oscillatory behaviour represented by $\mathbf{V}, \theta \sim \exp(i\omega t)$, then the right-hand sides of (B 1) and (B 2) will contain the terms $Pr\,\omega^2\beta\mathbf{V}$ and $w^2\beta\theta$, respectively, owing to the artificial second time derivatives. When the time oscillatory components of $\mathbf{V}$ and θ satisfy linear equations, it is evident that these terms represent an artificial amplification effect. For $Pr = 1$ and small β this amplification effect is approximately represented by the time variation $\exp(\sigma_r t)$ with σ_r given by $\sigma_r = \beta\omega^2$. In the present calculations with $Pr = 0{\cdot}7$ a similar type of amplification effect should be expected for linear disturbances. When the disturbances reach finite amplitude, it may be expected that the disturbance kinetic energy K' will be increased owing to this artificial effect.

The values of the grid intervals Δx, Δy, Δz and Δt and of the parameters β, τ and $\beta\omega^2$ are given in table 5 for runs A–$F1$. For runs A and B the values of τ were estimated from the observed time variation of individual cells which formed and decayed before the flow approached the asymptotic two-dimensional steady state. The values of τ for runs C, F and $F1$ were obtained from the finite amplitude travelling wave disturbances. The values $\tau = 0{\cdot}24$ and $\tau = 0{\cdot}45$ for run D and the range of values $0{\cdot}05 < \tau < 0{\cdot}20$ for run E were discussed in § 5.

The magnitude of $\beta\omega^2$ for runs A–$F1$ shown in table 5 gives some indication of the possible importance of the DuFort–Frankel time truncation error in the various runs. $\beta\omega^2$ has its largest magnitudes for the more rapidly moving disturbances in runs D and E. The dashed lines in figure 7 for $Ra = 9000$ and in figure 10 for $Ra = 25\,000$ show the effect of halving the time step in these plots of w and θ *vs.* time. It is seen that the amplitude of the disturbances is virtually unchanged by increasing the time resolution, but there is an apparent slight decrease in the period of the oscillations. These results suggest that the DuFort–Frankel error has minor importance for these runs. A comparison of the flow fields and the integrated statistics for the two different time resolutions indicates the same conclusion.

Run	Ra	Δx	Δy	$\Delta z \times 10$	$\Delta t \times 10^3$	$\beta \times 10^3$	τ	$\beta\omega^2$
A	4 000	0·1364	0·1364	0·6250	2·40	2·09	~4·0	0·005
B	4 000	0·1667	0·1667	0·7143	2·40	1·54	~1·7	0·021
C	6 500	0·1429	0·1600	0·7143	1·20	0·409	0·28	0·206
D	9 000	0·1111	0·1094	0·5556	0·90	0·396	0·24	0·271
							0·45	0·077
E	25 000	0·0975	0·0975	0·5000	0·50	0·153	0·05–0·20	2·41–0·151
F	6 500	0·1000	0·1000	0·5000	0·80	0·384	0·27	0·208
$F1$	6 500	0·1000	0·1000	0·5000	0·40	0·096	0·27	0·052

TABLE 5. Values of the grid intervals Δx, Δy, Δt and of β, τ, $\beta\omega^2$ for runs A–$F1$. The frequency ω is related to the period τ by $\omega = 2\pi/\tau$. The quantity β is defined in (B 3).

	Run C	Run F	Run $F1$
K	89·46	86·88	86·70
$\bar{K}$	59·59	59·57	62·80
K'	29·87	27·31	23·90

TABLE 6. The values of K, $\bar{K}$ and K' for runs C, F and $F1$

Detailed information concerning space and time truncation errors for runs C, F and $F1$ is given in table 6. The data for run C were obtained at the end of this run. The values of $\bar{K}$ and K' given for runs F and $F1$ are the extrapolated values calculated at the ends of these runs.

When these three runs are compared, it is seen that the values of $\beta\omega^2$ are virtually identical for runs C and F. Thus run F has a higher space resolution than run C but the same time resolution. Run $F1$ has the same space resolution as run F but double the time resolution. The data in table 6 indicate that K' is reduced by both higher space and higher time resolution. That K' is significantly increased owing to time truncation is an apparent result of the DuFort–Frankel time truncation error.

The total kinetic energy K, however, is much less sensitive to space and time truncation errors. The decrease in K from run C to run F due to improved space resolution is 3 %. The decrease in K from run F to run $F1$ due to improved time resolution is negligible. Thus the essential effect of higher time resolution is to reduce K' with a compensating increase in $\bar{K}$. The total decrease of K' from run C to run $F1$ is about 25 %. The value of K' is sensitive to numerical truncation errors apparently because $Ra = 6500$ is near the critical value of Ra for the onset of the present three-dimensional disturbances.

REFERENCES

BROWN, W. 1973 Heat-flux transitions at low Rayleigh number. *J. Fluid Mech.* **60**, 539.

BUSSE, F. H. 1972 The oscillatory instability of convection rolls in a low Prandtl number fluid. *J. Fluid Mech.* **52**, 97.

BUSSE, F. H. & WHITEHEAD, J. A. 1974 Oscillatory and collective instabilities in large Prandtl number convection. *J. Fluid Mech.* **66**, 67.

CHANDRASEKHAR, S. 1961 *Hydrodynamic and Hydromagnetic Stability.* Oxford: Clarendon Press.

CLEVER, R. M. & BUSSE, F. H. 1974 Transition to time-dependent convection. *J. Fluid Mech.* **65**, 625.

DEARDORFF, J. W. & WILLIS, G. E. 1967 Investigation of turbulent thermal convection between horizontal plates. *J. Fluid Mech.* **28**, 675.

KRISHNAMURTI, R. 1970*a* On the transition to turbulent convection. Part 1. The transition from two- to three-dimensional flow. *J. Fluid Mech.* **42**, 295.

KRISHNAMURTI, R. 1970*b* On the transition to turbulent convection. Part 2. The transition to time-dependent flow. *J. Fluid Mech.* **42**, 309.

KRISHNAMURTI, R. 1973 Some further studies on the transition to turbulent convection. *J. Fluid Mech.* **60**, 285.

LIPPS, F. B. & SOMERVILLE, R. C. J. 1971 Dynamics of variable wavelength in finite-amplitude Bénard convection. *Phys. Fluids*, **14**, 759.

PIACSEK, S. A. & WILLIAMS, G. P. 1970 Conservation properties of convection difference schemes. *J. Comp. Phys.* **6**, 392.

RICHTMYER, R. D. & MORTON, K. W. 1967 *Difference Methods for Initial Value Problems*, 2nd edn. Interscience.

SOMERVILLE, R. C. J. 1973 Numerical simulation of small-scale thermal convection in the atmosphere. *Proc. 3rd Int. Conf. Numerical Methods in Fluid Dyn.*, vol. 2. Springer. (*Lecture Notes in Physics*, vol. 19, pp. 238–245.)

SOMERVILLE, R. C. J. & LIPPS, F. B. 1973 A numerical study in three space dimensions of Bénard convection in a rotating fluid. *J. Atmos. Sci.* **30**, 590.

WILLIAMS, G. P. 1969 Numerical integration of the three-dimensional Navier–Stokes equations for incompressible flow. *J. Fluid Mech.* **37**, 727.

WILLIS, G. E. & DEARDORFF, J. W. 1967 Development of short-period temperature fluctuations in thermal convection. *Phys. Fluids*, **10**, 931.

WILLIS, G. E. & DEARDORFF, J. W. 1970 The oscillatory motions of Rayleigh convection. *J. Fluid Mech.* **44**, 661.

WILLIS, G. E., DEARDORFF, J. W. & SOMERVILLE, R. C. J. 1972 Roll-diameter dependence in Rayleigh convection and its effect upon the heat flux. *J. Fluid Mech.* **54**, 351.